Volume 17
Number 6
14 February 2025
Pages 2915-3520

Nanoscale

rsc.li/nanoscale

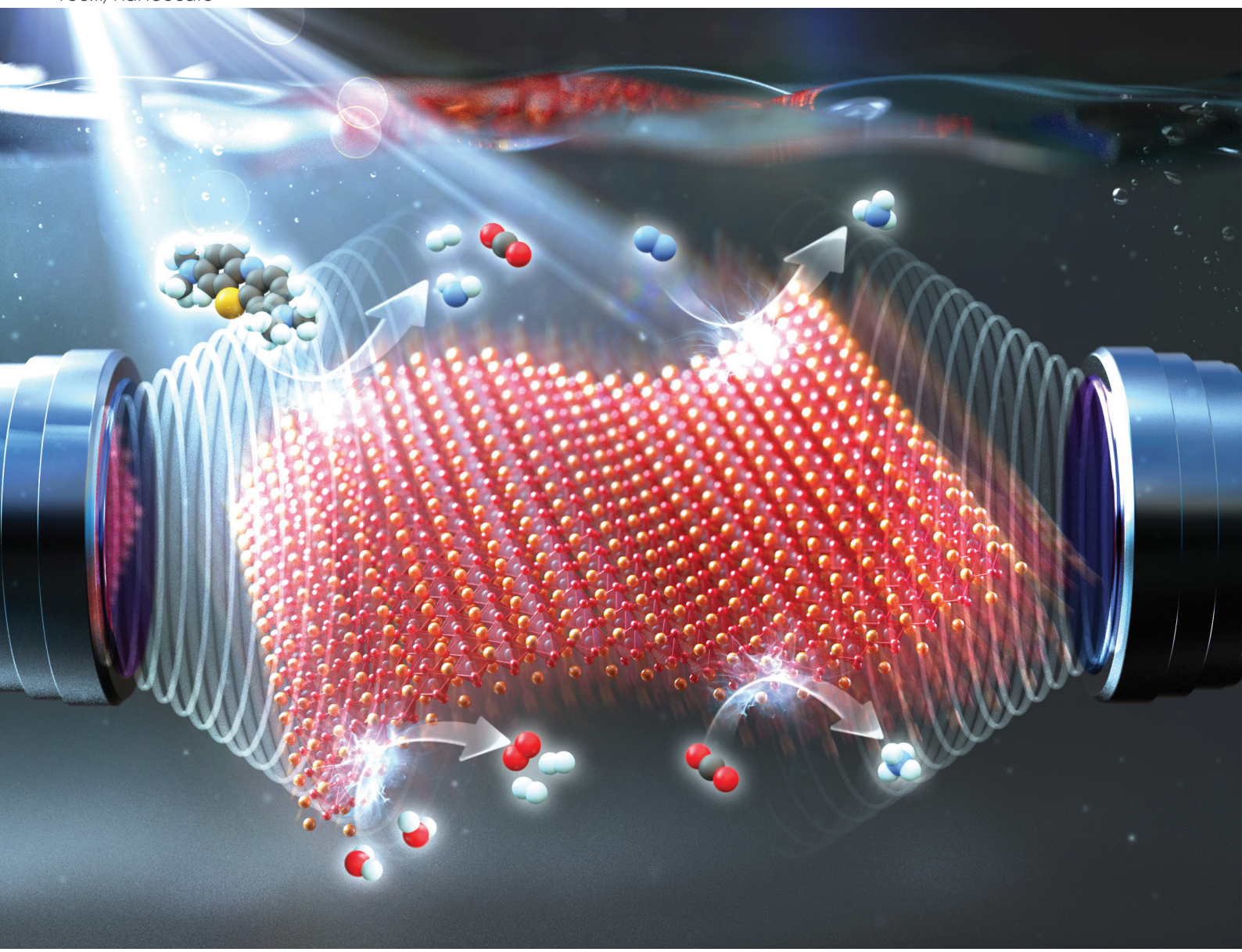

ISSN 2040-3372

ROYAL SOCIETY OF CHEMISTRY

REVIEW ARTICLE

Jong Wook Roh, Yuho Min *et al.*

Strategic design of emerging (K,Na)NbO_3-based perovskites for high-performance piezocatalysis and photo-piezocatalysis

NCNST

Nanoscale

REVIEW

View Article Online
View Journal | View Issue

Cite this: *Nanoscale*, 2025, **17**, 2931

Strategic design of emerging (K,Na)NbO_3-based perovskites for high-performance piezocatalysis and photo-piezocatalysis

Seonhwa Park,†[a] Hui Yong Jeong,†[a,b,c,d] Seokhwan Kim,[a,b,c,d] Mahesh Peddigari,[e] Geon-Tae Hwang,[f] Geon Dae Moon,[g] Jong Wook Roh*[a,h] and Yuho Min*[a,b,c,d]

As a leading Pb-free perovskite material (ABO_3-type), potassium sodium niobate (K,Na)NbO_3 (KNN)-based ferroelectrics/piezoelectrics have been widely used in electronics, energy conversion, and storage due to their exceptional ability to interconvert mechanical and electrical energies. Beyond traditional applications, the piezoelectric potential generated by mechanical strain or stress modifies their energy band structures and facilitates charge carrier separation and transport, drawing increasing attention in emerging fields such as piezocatalysis and photo-piezocatalysis. With excellent piezoelectric properties, chemical/thermal stability, and strain-tuning capability, KNN-based materials show great promise for high-performance piezocatalytic applications. Coupling KNN with semiconductors exhibiting strong optical absorption to form heterojunctions further boosts performance by suppressing electron–hole recombination and promoting directed charge transfer, which is crucial for photo-piezocatalysis. The flexibility of KNN's perovskite structures also allows for modifications in chemical composition and crystal structure, enabling diverse design strategies such as defect engineering, phase boundary engineering, morphology control, and heterojunction formation. This review comprehensively explores the recent advancements in KNN-based piezocatalysis and photo-piezocatalysis, starting with an overview of their crystal structures and intrinsic properties. It then explores the role of piezoelectric potential in charge carrier dynamics and catalytic activity, followed by strategic design approaches to optimize efficiency in environmental remediation and energy conversion. Finally, the review addresses current challenges and future research directions aimed at advancing sustainable solutions using KNN-based materials in these applications.

Received 25th October 2024,
Accepted 11th December 2024

DOI: 10.1039/d4nr04415k

rsc.li/nanoscale

1. Introduction

Ferroelectrics are materials characterized by spontaneous electric polarization, which can be reversed by applying an external electric field. This property arises from asymmetry in their crystal structures, typically involving non-centrosymmetric ion arrangements that result in a permanent dipole moment.[1] Ferroelectrics exhibit spontaneous polarization even without an external electric field and their polarization response to an alternating electric field is represented by a hysteresis loop. Most ferroelectrics also exhibit piezoelectric properties, generating electric charge under mechanical stress or undergoing deformation when subjected to an electric field. Additionally, their high dielectric constants make them ideal for energy storage applications such as capacitors. Among lead-free ferroelectric materials, (K,Na)NbO_3 (KNN)-based perovskites have gained significant attention across various fields, including electronics, energy harvesting, and capacitors due to their excellent ferroelectric, piezoelectric, and dielectric properties.[2] KNN-based materials possess structural flexibility that allows for the incorporation of various cations into their perovskite structure. This flexibility enables compositional modulation and phase boundary engineering to further enhance their properties.[3]

In addition to traditional electronic applications, KNN-based ferroelectrics/piezoelectrics have emerged as promising

[a]*Regional Leading Research Center for Smart Energy System, Kyungpook National University, Daegu 41566, Korea. E-mail: jw.roh@knu.ac.kr, yuhomin@knu.ac.kr*
[b]*Department of Materials Science and Metallurgical Engineering, Kyungpook National University, Daegu 41566, Korea*
[c]*Innovative Semiconductor Education and Research Center for Future Mobility, Kyungpook National University, Daegu 41566, Korea*
[d]*Research Institute of Automotive Parts and Materials, Kyungpook National University, 80 Daehakro, Buk-gu, Daegu, Korea*
[e]*Department of Physics, Indian Institute of Technology Hyderabad, Kandi 502284, Telangana, India*
[f]*Department of Materials Science and Engineering, Pukyong National University, Busan 48513, Korea*
[g]*Dongnam Regional Division, Korea Institute of Industrial Technology, Busan 46938, Korea*
[h]*School of Nano and Materials Science and Engineering, Kyungpook National University, Sangju 37224, Korea*
†These authors contributed equally to this work.

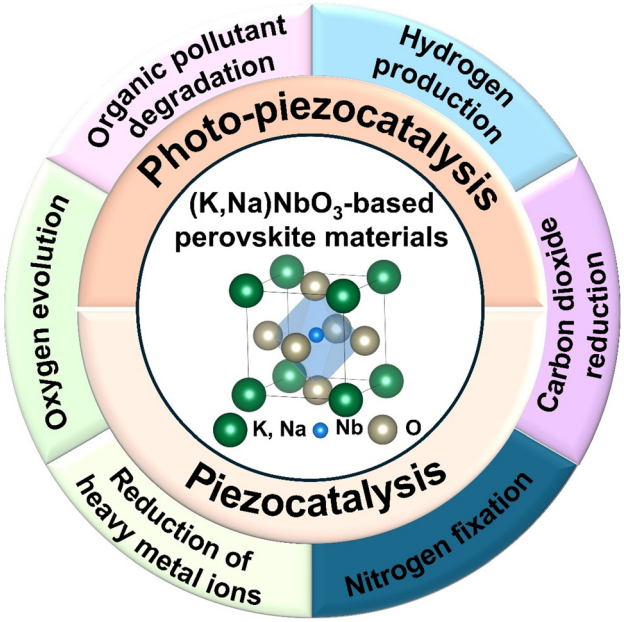

Scheme 1 Potential application fields of piezocatalysis and photo-piezocatalysis using (K,Na)NbO_3-based materials.

candidates for piezocatalysis and photo-piezocatalysis. These fields leverage the unique properties of these materials to drive catalytic reactions under mechanical stimuli (piezocatalysis) or combined light and mechanical stimuli (photo-piezocatalysis).[4] These processes are particularly promising for addressing energy and environmental challenges, such as organic pollutant degradation, water splitting, carbon dioxide reduction, nitrogen fixation, and reduction of heavy metal ions (Scheme 1).[5] Piezocatalysis operates by utilizing the piezoelectric potential generated when piezoelectric materials like KNN are subjected to mechanical stress (*e.g.* bending, compression, or vibration).[6] This strain-induced piezoelectric potential creates an internal electric field that promotes charge separation, driving redox reactions on the material's surface.[7] Sufficient mechanical stress can also excite electrons from the valence band to the conduction band, generating the charge carriers.[8] The piezoelectric potential tilts the energy band structure, facilitating efficient electron–hole separation, allowing them to participate in redox reactions, provided their energies align with specific reactions.[9] Beyond its energy efficiency and eco-friendliness, piezocatalysis offers the unique advantage of functioning without external heat or electricity, making it particularly appealing for sustainable applications. Photo-piezocatalysis combines mechanical strain with light irradiation to further enhance catalytic activity.[10] This dual-stimulus approach leverages both piezoelectric potential and photo-excited charge carriers, significantly improving charge separation and reducing electron–hole recombination, which enhances overall catalytic efficiency.[11] KNN-based materials, known for their higher piezoelectric coefficients compared to other Pb-free perovskites such as $BaTiO_3$ and $Na_{0.5}Bi_{0.5}TiO_3$, are particularly effective in piezocatalysis.[12] Beyond their high piezoelectric coefficients, KNN-based materials uniquely balance structural flexibility and eco-friendly characteristics, distinguishing them from conventional piezocatalysts.[13] Their lead-free composition meets the growing demand for sustainable materials, while their ability to undergo compositional tuning enables the optimization of catalytic performance across diverse applications. This adaptability positions KNN-based systems as a promising solution for pressing energy and environmental challenges, facilitating efficient charge carrier separation and reduced recombination losses. However, their wide bandgap often limits their catalytic activity under light irradiation alone. By combining mechanical and light stimuli, photo-piezocatalysis can boost their catalytic efficiency, particularly when coupled with narrow bandgap semiconductors that enhance charge separation and mitigate recombination issues.[14]

A variety of materials, including ZnO, $ZnSnO_3$, MoS_2, $BaTiO_3$, $PbTiO_3$, $Pb(Zr,Ti)O_3$, $Pb(Mg_{1/3}Nb_{2/3})$–$PbTiO_3$, $BiFeO_3$,[15–22] have been explored for piezocatalysis and photo-piezocatalysis.[23–28] To enhance catalytic activities, researchers have employed strategies such as doping modulation, morphology control, heterojunction formation, metal loading/

Seonhwa Park

Seonhwa Park received her Ph. D. degree in 2023 from the Department of Materials Science and Engineering at Pusan National University. She is currently working as a postdoctoral fellow at the Regional Leading Research Center for Smart Energy System at Kyungpook National University. Her current interests focus on the design of ferroelectric/piezoelectric Pb-free perovskite materials for energy harvesting, storage, and catalysis applications.

Hui Yong Jeong

Hui Yong Jeong received his B.S. in 2023 from the Department of Materials Science and Metallurgical Engineering at Kyungpook National University. He is currently pursuing his M.S. degree under the supervision of Prof. Yuho Min in the same department. His research interests include the synthesis of single-crystal Pb-free perovskites and their applications in energy and environmental fields.

deposition, defect engineering, phase boundary engineering, strain engineering, and combining with other reactions.[29–42] Doping modulation, in particular, has proven to be one of the most effective methods, allowing precise control over electronic and structural properties to optimize catalytic performance.[43] For instance, single-Ca doping in nitrogen-doped carbon, coupled with a PVDF membrane, enhanced piezocatalytic efficiency by improving β-phase formation and generating reactive oxygen species (ROS).[44] Similarly, Na and Sm co-doping in $SrBi_2Nb_2O_9$ strengthened internal electric fields, improved light absorption, and enhanced anisotropic charge migration, facilitating pollutant removal.[45] Morphology control also plays a critical role; for example, 2D $BaTiO_3$ nanosheets demonstrated superior piezocatalytic activity compared to their 0D and 1D counterparts due to their enhanced piezoelectric potential under mechanical vibration.[30] A $Bi_4Ti_3O_{12}$(BTO)@Carbon heterojunction also showed improved photo-piezoelectric activity for RhB degradation, where the heterojunction formation and piezoelectric potential synergistically enhanced electron transfer.[32] Similarly, Pd nanoparticle deposition on $BiFeO_3$ significantly increased hydrogen evolution under ultrasound vibration by facilitating charge carrier separation.[34] Oxygen vacancy in $BaTiO_3$ nanobelts improved organic dye degradation by enhancing superoxide radical production, although excessive vacancies can reduce piezoelectric performance.[35] Furthermore, phase boundary formation in $AgNbO_3$–$LiTaO_3$ solid solution led to improved piezoelectric and photo-piezocatalytic activities.[38] Nb doping on $Bi_4Ti_3O_{12}$ nanosheets also boosted photo-piezocatalytic CO_2 reduction, driven by strain-induced polarization enhancement.[40] While these strategies have been successfully applied to various materials, their application to KNN-based piezo-/photo-piezocatalysts remains relatively unexplored. Future research efforts should focus on adapting and optimizing these approaches to further advance the development of high-performance KNN-based materials for diverse catalytic applications.

Recently, numerous high-quality review papers have been dedicated to advancing the understanding of piezocatalysis and photo-piezocatalysis, with a focus on fundamental mechanisms, synthetic approaches, and emerging novel piezocatalysts.[46–50] Additionally, various review articles have explored key design strategies, including defect engineering, heterojunction formation, and metal deposition.[51–57] From an application standpoint, some reviews have concentrated on specific areas, such as biomedical applications, environmental remediation, hydrogen evolution, H_2O_2 production, and CO_2 reduction.[58–67] Despite this progress, relatively few studies have focused on KNN-based piezo- and photo-piezocatalysts. Given the promising properties of KNN-based materials, including excellent ferroelectric properties, chemical/thermal stability, and environmental compatibility, further research is needed to optimize its catalytic performance. Notably, polarized $K_{0.5}Na_{0.5}NbO_3$ has already demonstrated a 7.4-fold enhancement in photocatalytic hydrogen evolution, indicating the significant potential of KNN-based materials in energy and environmental applications.[68]

This review highlights recent advancements in KNN-based piezocatalytic and photo-piezocatalytic systems across a range of practical applications. The discussion primarily emphasizes intrinsic properties, catalytic performance, and material optimization strategies under mechanical and light stimuli. While external factors, such as the use of oxidants like persulfate, peroxymonosulfate, and H_2O_2, play a significant role in advanced oxidation processes, these aspects are beyond the scope of this review. Instead, this work aims to comprehensively understand material-oriented advancements in KNN-based piezocatalysis and photo-piezocatalysis. For this, we begin with a fundamental overview of KNN-based perovskites, focusing on their crystal structure and ferroelectric/piezoelectric properties. We then explore the theoretical principles underpinning piezocatalysis and photo-piezocatalysis, followed by a discussion of various strategies to enhance the catalytic performance of KNN-based materials, including

Jong Wook Roh

Jong Wook Roh obtained his PhD from Yonsei University in 2011. And he researched at Samsung Advanced Institute of Technology from 2011 to 2018. Now, he works at Kyungpook National University as an associate professor since 2018. His main research activities are concerned with synthesis of nanostructured materials and devices.

Yuho Min

Yuho Min received his B.S. in 2010 and Ph. D. in 2015 from the Department of Materials Science and Engineering at Yonsei University. He then worked as a professional researcher at LG Chem Research Park (2015–2017) before moving to the Functional Ceramics Department at the Korea Institute of Materials Science, where he served as a senior researcher (2017–2022). In 2022, he joined the Department of Materials Science and Metallurgical Engineering at Kyungpook National University as an assistant professor. His research interests include designing functional materials and their energy and environmental applications.

phase boundary engineering, defect engineering, morphology control, heterojunction formation, metal deposition/loading, and modulation of external condition. Finally, we address key challenges and propose future research directions aimed at advancing these KNN-based materials for diverse catalytic applications.

2. Fundamental overview of (K,Na) NbO_3-based perovskites

2.1. Crystal structure

Potassium sodium niobate (K,Na)NbO_3 (KNN) perovskites are promising Pb-free materials, primarily consisting of a solid solution of $KNbO_3$ (KN) and $NaNbO_3$ (NN). Like other perovskite oxides, KNN-based materials adopt the general formula ABO_3, with K^+/Na^+ ions at the A-site and Nb^{5+} ions at the B-sites. In the cubic structure, K^+/Na^+ ions are located at the corners, coordinated to twelve oxygen atoms, while Nb^{5+} ions are at the body center, coordinated to six oxygen atoms, forming corner-sharing NbO_6 octahedra (Fig. 1(a)). KNN perovskites exhibit structural and compositional flexibility, enabling the incorporation of various cations with diverse oxidation states into the A- and B-sites while maintaining their perovskite structure with a high degree of stability.[69] Doping cations with different radii and oxidation states can induce lattice distortion and create vacancies to maintain charge neutrality, leading to changes in the crystal structure and surface charge redistribution.[70] The tilting of NbO_6 octahedron affects ionic displacement, influencing their ferroelectric/piezoelectric properties, as well as piezocatalytic activity.[71] The stability of perovskite structure is commonly estimated using the Goldschmidt tolerance factor (t), expressed as follows:

$$t = \frac{(R_A + R_O)}{\sqrt{2}(R_B + R_O)} \quad (1)$$

where, R_A, R_B, and R_O are the radius of A, B, and O ions, respectively.[72] A perfect cubic perovskite has a tolerance factor

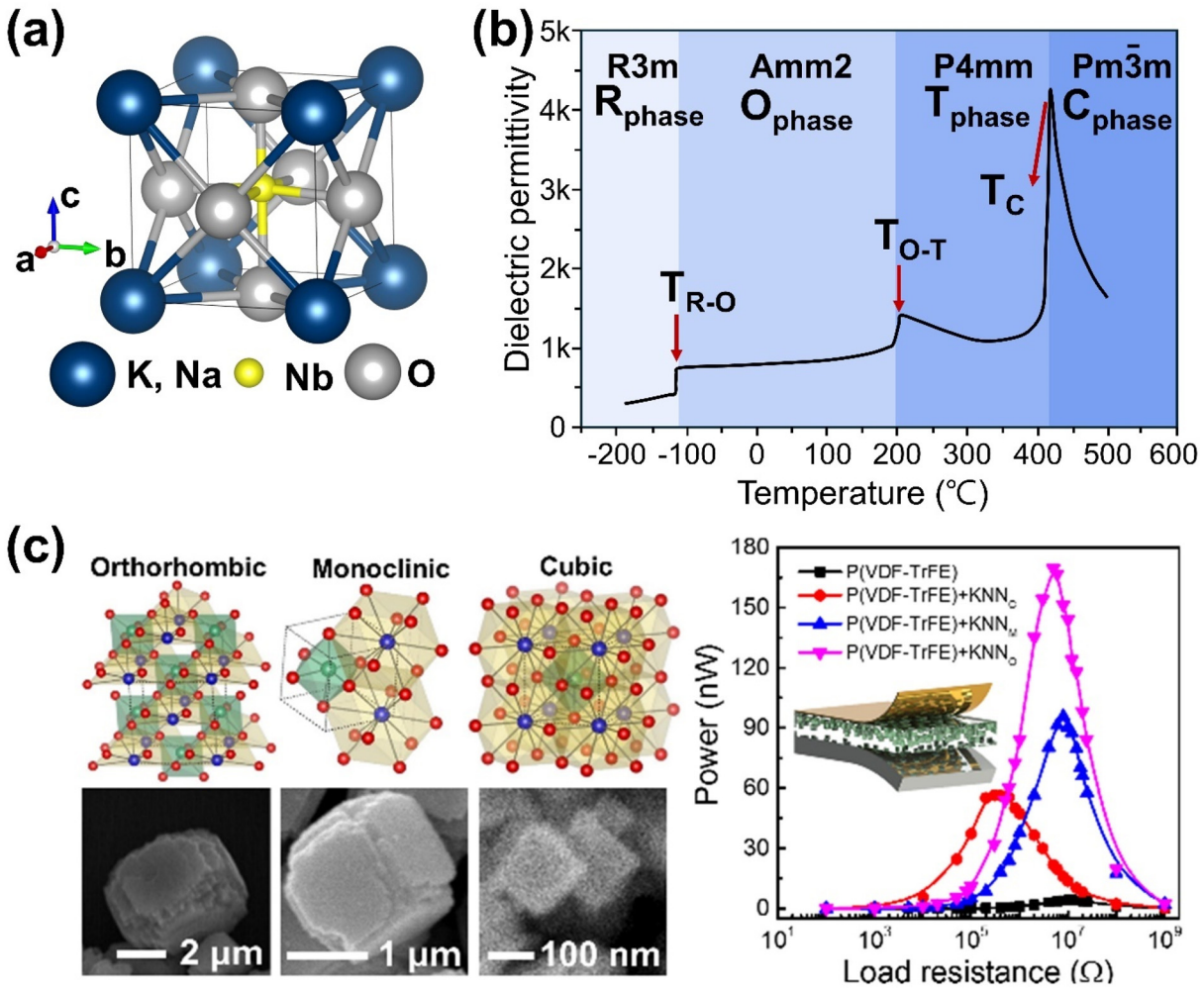

Fig. 1 (a) Crystal structure and (b) temperature-dependent dielectric permittivity of undoped (K,Na)NbO_3 perovskites. (c) Selective phase control of three different phased (K,Na)NbO_3 particles prepared by hydro/solvothermal methods and their corresponding energy harvesting performance. Reprinted with permission from ref. 75. Copyright 2020, American Chemical Society.

of 1, but in reality, most KNN-based materials deviate from this value due to the tilting of NbO_6 units, which is influenced by factors such as composition, temperature, strain, and polarization.[73] Undoped KNN undergoes polymorphic phase transition depending on composition (*i.e.*, the molar ratio of KN and NN) and temperature. For instance, $K_{0.5}Na_{0.5}NbO_3$ ceramics exhibit three phase transitions from rhombohedral ($R3m$) to orthorhombic ($Amm2$) at about −100 °C (T_{R-O}), orthorhombic to tetragonal ($P4mm$) near 200 °C (T_{O-T}), and tetragonal to cubic ($pm\bar{3}m$) above 400 °C (T_C: Curie temperature) (Fig. 1(b)).[74] Although the orthorhombic phase is most thermodynamically stable for undoped KNN, three different phases of pure KNN particles (orthorhombic, monoclinic, and cubic) have been successfully synthesized by adjusting hydro/solvothermal synthesis conditions. Additionally, PVDF-TrFE polymer composites containing these three KNN particles demonstrated structural-dependent mechanical energy harvesting performance (Fig. 1(c)).[75]

2.2. Ferroelectric and piezoelectric properties

The structural and compositional flexibility of KNN-based materials allows for tuning of their intrinsic properties, including ferroelectric, piezoelectric, piezocatalytic, and photo-piezocatalytic properties, band structure, and charge separation efficiency.[76] KNN-based perovskites are known for their promising ferroelectric/piezoelectric properties. Within their NbO_6 octahedra, Nb^{5+} ions tend to shift slightly from the center due to asymmetric ion arrangement, creating local electric dipoles. When these dipoles align collectively, KNN-based materials exhibit large spontaneous polarization, a key characteristic of ferroelectricity. When mechanical stress is applied, the dipoles realign, producing an electric field, which is the piezoelectric effect. The strong ferroelectric polarization in KNN-based materials enhances their piezoelectric response, and the ease of domain reorientation boosts the piezoelectric sensitivity.

Several effective strategies have been employed to improve the piezoelectric properties of KNN-based materials. For instance, doping with ions such as Li^+, Ag^+, Ca^{2+}, Ba^{2+}, Bi^{3+}, Sb^{5+}, Ta^{5+}, Zr^{4+}, Hf^{4+}, or using ABO_3-type perovskites like $LiTaO_3$, $CaZrO_3$, $SrZrO_3$, $BaZrO_3$, $BiFeO_3$ can modify phase transition temperatures, enabling the coexistence of multiple phases and creating a polymorphic phase boundary (PPB) (Fig. 2(a)).[13,77,78] This phase boundary engineering improves piezoelectric properties by facilitating polarization rotation under stress. Another effective method to enhance piezoelectricity is through grain/domain alignment using templated grain growth (TGG), where oriented grain growth is achieved by using templates as nucleation sites.[79] Park *et al.* demonstrated improved piezoelectric properties in textured KNN-based ceramic, where aligned grains/domains contribute more to the piezoelectric response compared to randomly oriented polycrystalline ceramic counterparts (Fig. 2(b)).[80] Additionally, single crystals of KNN-based materials, which take advantage of their intrinsic anisotropy and polarization rotation, exhibit even greater piezoelectric properties.[81] Park *et al.* found that KNN-based single-crystal microcubes synthesized by the molten-salt method exhibited better piezoelectric properties than ceramics with the same composition (Fig. 2(c)).[82]

2.3. Piezoelectric potential

Undoubtably, the piezoelectric properties are crucial for generating a piezoelectric potential (V_p), under mechanical stress. This potential is expressed as:[72]

$$V_p = \frac{P_i W_i}{\varepsilon_o \varepsilon_{ri}} = \frac{d_{ij} T_j W_i}{\varepsilon_o \varepsilon_{ri}} \quad (2)$$

Where V_p, P_i, W_i, d_{ij}, T_j, ε_o, and ε_{ri} are the piezoelectric potential, piezoelectric polarization generated in dimension i, width of the material in dimension i, piezoelectric coefficient (pC/N), stress applied in the dimension j, dielectric constant of a vacuum, and relative permittivity in dimension i.[83] This piezoelectric potential induces internal polarization states within the materials, facilitating the involvement of adsorbed external charge carriers in the desired redox reactions.[46] It also acts as a driving force for transferring electrons and holes to reactant molecules adsorbed on the surface.[84] The piezoelectric coefficient (d_{33}), proportional to the piezoelectric potential, is a critical factor in determining catalytic performance. KNN-based materials, through doping and phase boundary engineering, have achieved d_{33} values exceeding 400 pC/N in designed compositions, significantly higher than other lead-free piezoceramics like $BaTiO_3$ and $BiNaTiO_3$, which typically range between 200–300 pC/N.[78] These advancements make KNN a highly promising candidate for piezocatalytic applications, especially when the high piezoelectric response is essential for effective charge separation. Moreover, doping elements such as Li, Sb, and Ta help to create a polymorphic phase boundary (PPB), further enhancing piezoelectric performance by stabilizing multiple-phase coexistence at room temperature.[85] Even though KNN-based materials have relatively wide band gaps (over 3.0 eV), the high piezoelectric coefficients and resulting piezoelectric potential effectively reduce charge recombination and facilitate the separation of photo-excited charges, a common issue in traditional photocatalysis.[86] Therefore, KNN-based materials with high piezoelectric coefficients are essential for generating strong piezoelectric potential, which is critical for enhancing both piezo- and photo-piezocatalytic performance by promoting charge separation, reducing recombination, and boosting overall catalytic activity.

3. Mechanism and theory of piezocatalysis and photo-piezocatalysis

Piezocatalysis, the process of converting mechanical energy into chemical energy, has garnered significant attention due to its potential applications in environmental remediation, hydrogen production, and other catalytic applications. When combined with photocatalysis, the synergistic effect of photo-piezocatalysis significantly enhances catalytic efficiency by

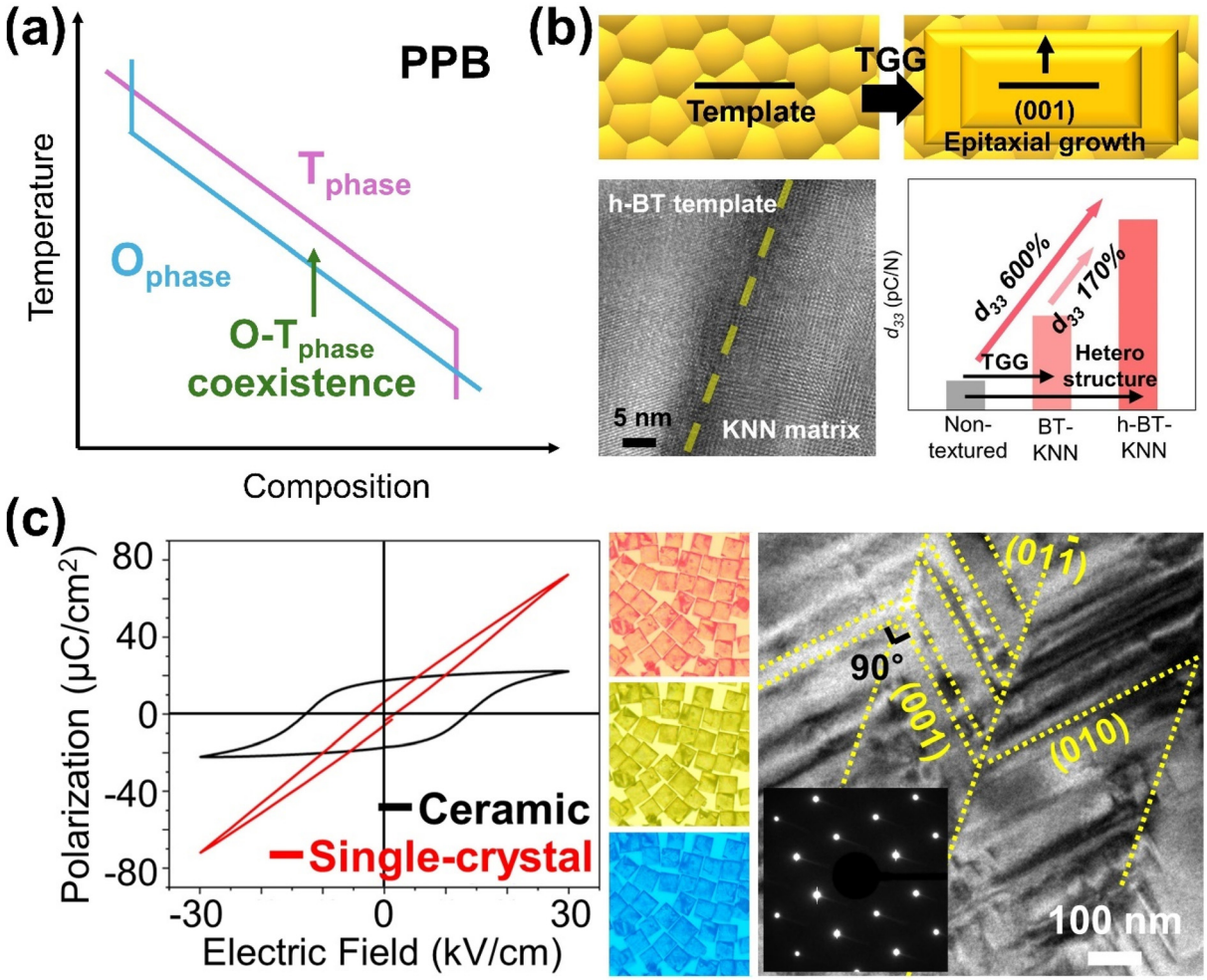

Fig. 2 (a) Schematic on polymorphic phase transition (PPB). (b) Schematic drawing of templated grain growth (TGG) together with a comparison of piezoelectric constants (d_{33}) of KNN-based non-textured and textured ceramics and representative HR-TEM image showing the interface between BT template and KNN matrix in textured KNN ceramics. Reprinted with permission from ref. 80. Copyright 2023, Elsevier. (c) Optical microscope and HR-TEM images of single-crystal KNN microcubes together with a comparison of polarization–electric field (P–E) curves between the same compositional single-crystal KNN microcube and polycrystalline KNN-based ceramic. Reprinted with permission from ref. 82. Copyright 2022, American Chemical Society.

integrating mechanical and light energy. The fundamental mechanisms behind these catalytic processes are explained by two complementary theories: (i) energy band theory and (ii) screening charge theory. These theories provide insights into how mechanical deformation in piezoelectric materials induces catalytic activity.

3.1. Energy band theory

In energy band theory, mechanical stress or vibrations in piezoelectric materials generate a piezoelectric potential, which causes tilting of the conduction band (CB) and valence band (VB) (Fig. 3). The CB shifts to a more negative potential, facilitating more efficient electron transfer for reduction reactions, while the VB shifts positively, enabling oxidation reactions. The direction of CB and VB shifts depends on the polarization induced by piezoelectric potential. Without strain, the CB and VB remain aligned horizontally (Fig. 3(a)). Upon polarization, electrons migrate and accumulate on the positive side while holes move to the negative side, resulting in downward and upward band tilts, respectively (Fig. 3(b)). This band tilting spatially separates charge carriers, reducing their recombination, and allowing electrons and holes to migrate to the surface where they participate in redox reactions, such as generating reactive oxygen species (ROS).[46,55] This band tilting mechanism is particularly beneficial for reactions that are otherwise hindered due to unfavorable band edge positions in the absence of the piezoelectric effect. For example, Im *et al.* used KNN/CuO micro/nano heterostructures for piezo- and photo-piezocatalytic dye degradation.[4] Under light irradiation alone, the VB of CuO is insufficiently positive to drive the $OH^-/^{\bullet}OH$ redox reaction (1.90 V). However, under periodic mechanical vibration, piezoelectric potential shifts the band positions of KNN/CuO, making the VB of CuO more positive than the $OH^-/^{\bullet}OH$ redox potential, resulting in significantly

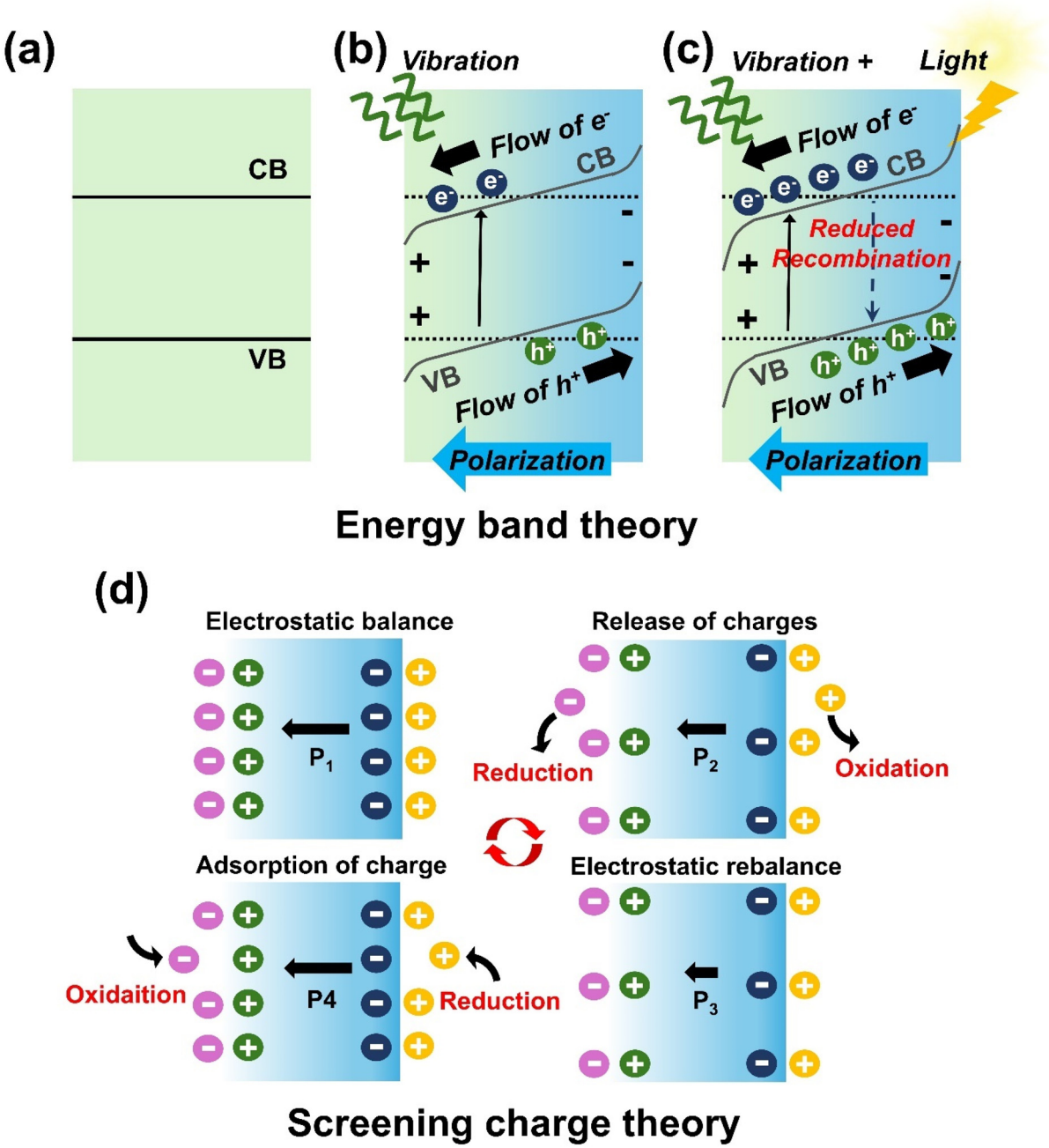

Fig. 3 Schematic illustrations of energy band structure (a) in the absence of mechanical stimuli (b) under mechanical stress, and (c) under both mechanical and light irradiation. (d) Schematic representation of the screening charge theory showing release and adsorption of surface charges depending on the polarization developed in a piezoelectric material.

improved dye degradation efficiency. One limitation of this theory is that piezoelectric materials, typically dielectrics with large band gaps, lack sufficient free-charge carriers. Free carriers are often generated under extreme conditions such as high pressure or thermal excitation during ultrahigh sonication.[87] Previous studies show that ultrasound-induced cavitation collapse can produce extremely high pressures (up to 10^8 Pa) and localized temperatures (4000–5000 °C) at the catalyst–water interface.[88] In photo-piezocatalysis, the piezoelectric potential further enhances charge separation efficiency from light irradiation, reducing recombination losses and improving overall catalytic performance (Fig. 3(c)).

3.2. Screening charge theory

The screening charge theory focuses on the interaction between polarization-induced charges within the piezoelectric material and external screening charges from the surrounding environment. Unlike energy band theory, which emphasizes

internal charge migration, this theory attributes catalytic activity to the redistribution of external charges on the surface of the piezoelectric material. Under constant mechanical stress, polarization-induced charges near the material's surface reach equilibrium with external screening charges. When the external stress is released, this equilibrium is disturbed, releasing excess screening charges that participate in surface redox reactions. A new equilibrium state is then established. As stress is reapplied, a new imbalance occurs, attracting more screening charges to the surface, where they accumulate and trigger further redox reactions (Fig. 3(d)). For effective catalytic reactions, the magnitude of piezoelectric potential must match the target redox potential.[89] In photo-piezocatalysis, the piezoelectric potential enhances the accumulation and mobility of screening charges at the surface. This combined with photo-generated carriers, drives redox reactions more efficiently.

3.3. Comparison of energy band theory and screening charge theory

While both energy band theory and screening charge theory provide explanations for piezocatalysis and photo-piezocatalysis, they differ in their emphasis on charge generation and migration. Energy band theory emphasizes intrinsic charge dynamics, wherein the piezoelectric potential generated by mechanical stress tilts the conduction band (CB) and valence band (VB). The degree of band tiling is proportional to the magnitude of piezoelectric potential induced by external mechanical stress, enabling thermodynamically unfavorable redox reactions by shifting the electronic energy band positions to more favorable locations. A notable example is observed in the $MoS_2/NaNbO_3$ heterojunction for piezocatalytic organic removal.[90] In the absence of mechanical stress, the valence band (VB) of MoS_2 is more negative than the redox potential of $^{\bullet}OH/H_2O$, preventing the generation of hydroxyl radicals. According to energy band theory, unlike photocatalysis, which requires appropriately aligned band edge positions, piezocatalysis overcomes this limitation through band shifting. Under the influence of the piezoelectric potential, the VB of MoS_2 shifts to a more positive position than the $^{\bullet}OH/H_2O$ redox potential, facilitating the desired reactions.

In contrast, screening charge theory focuses on the interaction between the polarization-induced charges within the piezoelectric material and external screening charges from the surrounding medium. Mechanical deformation generates a piezoelectric potential that disturbs the equilibrium of surface charges, attracting external screening charges from the environment. These charges accumulate on the surface and directly participate in redox reactions. For instance, the organic removal efficiency of $MoS_2/NaNbO_3$ was significantly reduced in the presence of external ions (Cl^-, CO_3^{2-}, and SO_4^{2-}) compared to the $MoS_2/NaNbO_3$ without external ions. This reduction occurs because the external ions in aqueous solutions screen the piezoelectric potential, thereby hindering its catalytic effect.[90] Unlike energy band theory, which relies on intrinsic charge carriers, screening charge theory highlights the role of externally sourced charges and surface phenomena, making it particularly relevant in systems with strong polarization and electrolyte interactions.

While both theories rely on the piezoelectric potential to drive catalytic activity, their mechanisms are fundamentally different. Energy band theory is intrinsic and material-centric, focusing on internal carrier dynamics and band alignment. In contrast, screening charge theory is surface-centric, emphasizing external interactions and surface charge redistribution. A recent study suggests that both mechanisms can operate simultaneously, with their relative contributions depending on the material properties such as piezoelectricity, band gap, and external excitation conditions (mechanical stress or light).[84] These theories often work synergistically in piezocatalysis, where band tilting enhances intrinsic charge separation, and surface screening charges further facilitate redox reactions. This synergy maximizes catalytic efficiency, making both theories essential for understanding and optimizing piezoelectric materials for diverse catalytic applications.

4. Optimization strategies for enhancing piezo- and photo-piezocatalytic activities

Optimizing KNN-based piezocatalytic and photo-piezocatalytic systems is essential to enhance their efficiency in converting mechanical and light energies into chemical reactions. Various design strategies have been developed to overcome challenges such as poor charge separation, low catalytic efficiency, and limited mechanical energy conversion. These strategies aim to achieve high-performance catalytic activity and include phase boundary engineering, defect engineering, morphology control, heterojunction formation, metal deposition/loading, and modulation of external conditions (Fig. 4). Collectively, these approaches broaden the applications of KNN-based materials in areas such as environmental remediation, water splitting, CO_2 reduction and N_2 fixation.

4.1. Phase boundary engineering

Phase boundary engineering involves intentionally creating or manipulating interfaces between different crystallographic phases within a material. These phases, such as tetragonal, orthorhombic, rhombohedral, or cubic, possess distinct structural properties. Their coexistence creates a phase boundary where the material's performance can be significantly optimized. In KNN-based materials, a polymorphic phase boundary (PPB) can form when the rhombohedral-to-orthorhombic (R–O) and orthorhombic-to-tetragonal (O–T) phase transitions are shifted near room temperature.[91] The coexistence of these phases at the PPB boosts the relative dielectric permittivity, leading to a substantial rise in the piezoelectric constant (d_{33}), as these properties are directly proportional.[92] A higher piezoelectric constant allows the material to generate a stronger piezoelectric potential under mechanical stress, which is criti-

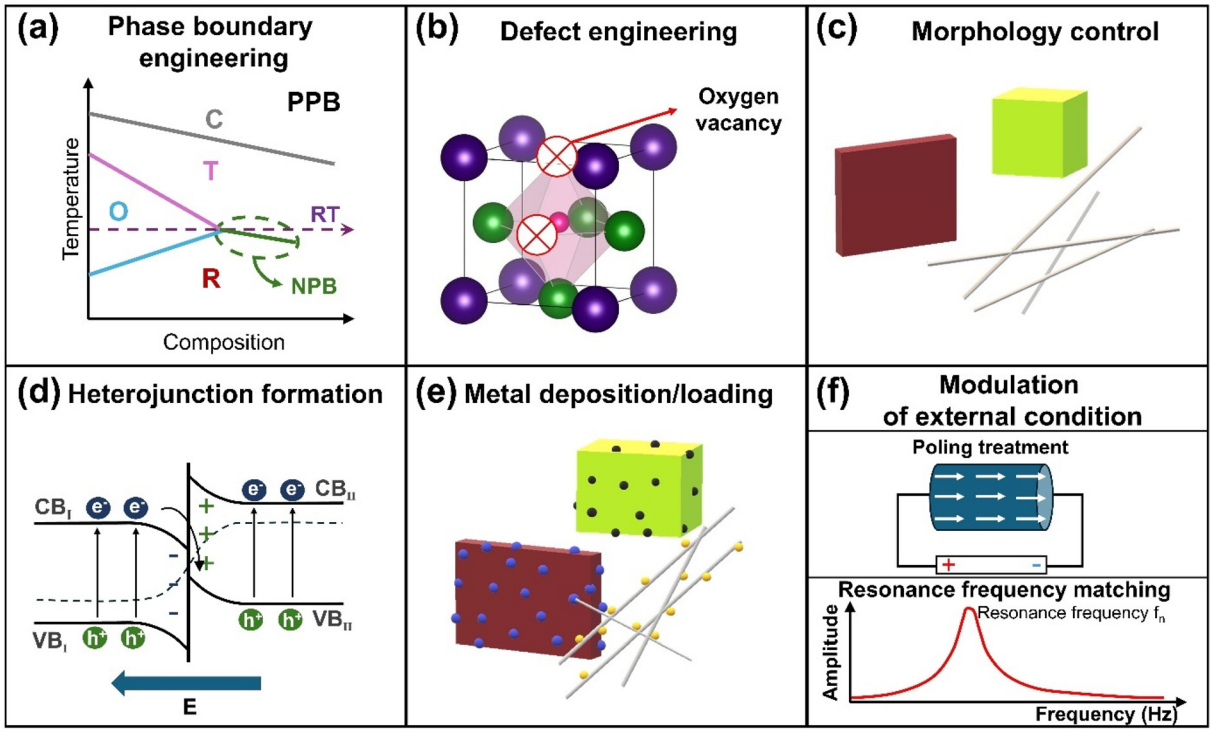

Fig. 4 Design strategies for improving piezocatalytic and photo-piezocatalytic activities of KNN-based materials. ((a) Phase boundary engineering, (b) Defect engineering, (c) Morphology control, (d) Heterojunction formation, (e) Metal deposition/loading, and (f) Modulation of external condition.

cal for driving piezocatalytic reactions. Phase boundary engineering is therefore pivotal in improving piezoelectric, dielectric, and catalytic properties of KNN-based materials, making it a key strategy for advancing their applications in piezocatalysis and photo-piezocatalysis.

For example, Fan *et al.* demonstrated that introducing a phase boundary between the orthorhombic and tetragonal phases in Li-doped $K_{0.5}Na_{0.5}NbO_3$ (KNN) significantly improved piezocatalytic activity.[8] The coexistence of these phases, achieved through Li doping, enhanced the piezoelectric response and the degradation of organic pollutants like RhB. A 6 mol% Li-doped KNN sample exhibited a 3.2-fold increase in piezocatalytic efficiency compared to pristine KNN, attributed to the optimized phase boundary that facilitates enhanced force-driven charge separation. Similarly, Wu *et al.* explored the modulation of polarization rotation through the creation of a multiphase coexistence of rhombohedral, orthorhombic, and tetragonal phases (R–O–T) in KNN-based materials, leading to improved piezocatalytic activity (Fig. 5(a)).[93] This multiphase coexistence lowered the energy barrier for polarization rotation, which in turn improved piezoelectric properties. The R–O–T phase coexistence yielded a 2.12-fold increase in the piezocatalytic reaction rate constant compared to materials with only an orthorhombic phase, understanding the critical role of phase boundary engineering in optimizing piezocatalytic performance.

Phase boundary engineering has also shown benefits for $NaNbO_3$ in both piezo- and photo-piezocatalysis. For instance, low-content Ba doping into $NaNbO_3$ induced a phase transition, leading to the coexistence of orthorhombic and cubic phases.[70] This phase boundary increased the number of active sites and improved charge separation, boosting the overall catalytic activity compared to single-phase $NaNbO_3$. Additionally, annealing-induced phase coexistence has been observed in $NaNbO_3$ nanowires.[94] By carefully controlling the annealing process (350 °C for 2 h), a coexistence of monoclinic, orthorhombic, and amorphous phases was achieved in the 350–2-NNO sample. The decreased structural symmetry at the two-phase interface improved piezoelectricity, while the increased oxygen vacancies in the amorphous structure promoted charge separation. When subjected to ultrasonic vibration, the deformation of the 350–2-NNO sample disrupted the electric equilibrium on the surface, initiating redox reactions that generated reactive oxygen species (ROS) for the degradation of antibiotics (Fig. 5(b)).

4.2. Defect engineering

Defect engineering, particularly through the creation of oxygen vacancies, plays a crucial role in optimizing piezocatalytic and photo-piezocatalytic systems. By modulating the electronic structure, carrier dynamics, and surface reactivity of the materials, oxygen vacancies enhance catalytic efficiency.[53] From a thermodynamic perspective, the formation of vacancies is energetically favorable, with their equilibrium concentration in the crystal determined by temperature.[95] Oxygen vacancies, which are missing oxygen atoms in the crystal

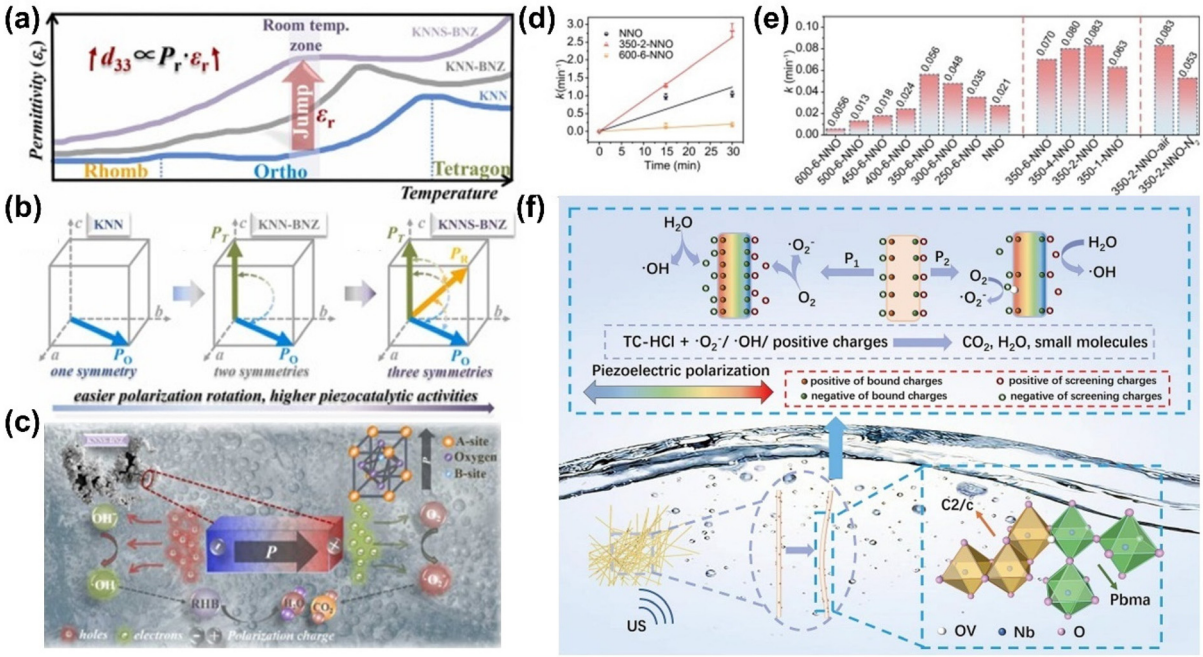

Fig. 5 (a and b) Schematic illustration of (a) temperature-dependent dielectric permittivity and (b) spontaneous polarization vector (P_s) of $(K_{0.5}Na_{0.5})NbO_3$ (KNN), $(K_{0.5}Na_{0.5})NbO_3$-$(Bi_{0.5}Na_{0.5})ZrO_3$ (KNN-BNZ), and Sb-doped $(K_{0.5}Na_{0.5})NbO_3$-$(Bi_{0.5}Na_{0.5})ZrO_3$ (KNNS-BNZ) samples. (c) Schematic illustration showing the generation of electrons and holes with their transfer for piezocatalysis. Reprinted with permission from ref. 93. Copyright 2022, Elsevier. (d) Pseudo-first-order kinetic fitting and (e) corresponding reaction rate constants of RC-HCl removal for $NaNbO_3$ nanowires annealed at different temperature, time, and atmospheres. (f) A proposed mechanism of piezocatalytic degradation of antibiotics by $NaNbO_3$ nanowires. Reprinted with permission from ref. 94. Copyright 2024, Elsevier.

lattice, typically produce localized electrons, increasing the charge carrier concentration. These free carriers facilitate more effective charge separation and migration under the influence of the piezoelectric potential, significantly improving catalytic reactions.[96]

However, excessive oxygen vacancies can act as pinning centers for domain wall motion, limiting domain mobility, and potentially reducing the piezoelectric response.[97] Careful control of oxygen vacancy concentration is therefore necessary to optimize both piezoelectric and catalytic properties. When introduced in controlled amounts, oxygen vacancies can modulate the internal electric field, enhancing polarization behavior. Additionally, defect dipoles formed by oxygen vacancies influence domain orientation, leading to improved piezoelectric response and mechanical-to-electrical conversion efficiency, which are critical for piezocatalysis.[98] Oxygen vacancies also serve as active sites that promote the adsorption and activation of reactants on the surface of materials. They lower the energy barrier for chemical reactions and support the formation of reaction intermediates, thus improving overall catalytic efficiency.[99] However, precise control of oxygen vacancies is key, as too many vacancies can negatively affect domain wall mobility and polarization.

In a recent study, Yang *et al.* prepared $NaNbO_3$ powders and annealed them in a nitrogen atmosphere to generate oxygen vacancies.[100] This process significantly enhanced the piezocatalytic efficiency, with the sample annealed 180 °C for 12 h showing a more than six-fold increase in efficiency compared to non-annealed samples. The oxygen vacancies improved the electronic structure by facilitating the excitation of valence electrons into the conduction band, which promoted better charge separation. Partial density of states (PDOS) analysis revealed that oxygen vacancies increased electron excitation probability from A-site Na atoms, while slightly reducing excitation from B-site Nb atoms (Fig. 6(a) and (b)). This improved charge carrier dynamics, particularly electron excitation at the A-site, while also enhancing charge transport at the B-site, contributing to improved piezocatalytic performance. Furthermore, the substitution of Nb with a moderate amount of FeCo (0.015 mol%) in KNN materials generated beneficial oxygen vacancies.[101] These vacancies pinned ferroelectric domains, leading to enhanced charge separation and reduced non-radiative recombination. The resulting internal field facilitated electron transport to the surface, where it promoted redox reactions.

In addition to thermal, chemical, and electrochemical reduction methods for generating oxygen vacancies, high-energy sand-grinding has also been shown to increase oxygen vacancy concentration in KNN-based materials (Fig. 6(c)).[102] Sand-ground KNN samples exhibited increased oxygen vacancies, leading to enhanced piezocatalytic performance. For example, the sand-ground-8 h sample showed the highest RhB degradation rate constant due to improved electron–hole pair separation and carrier mobility. These oxygen vacancies

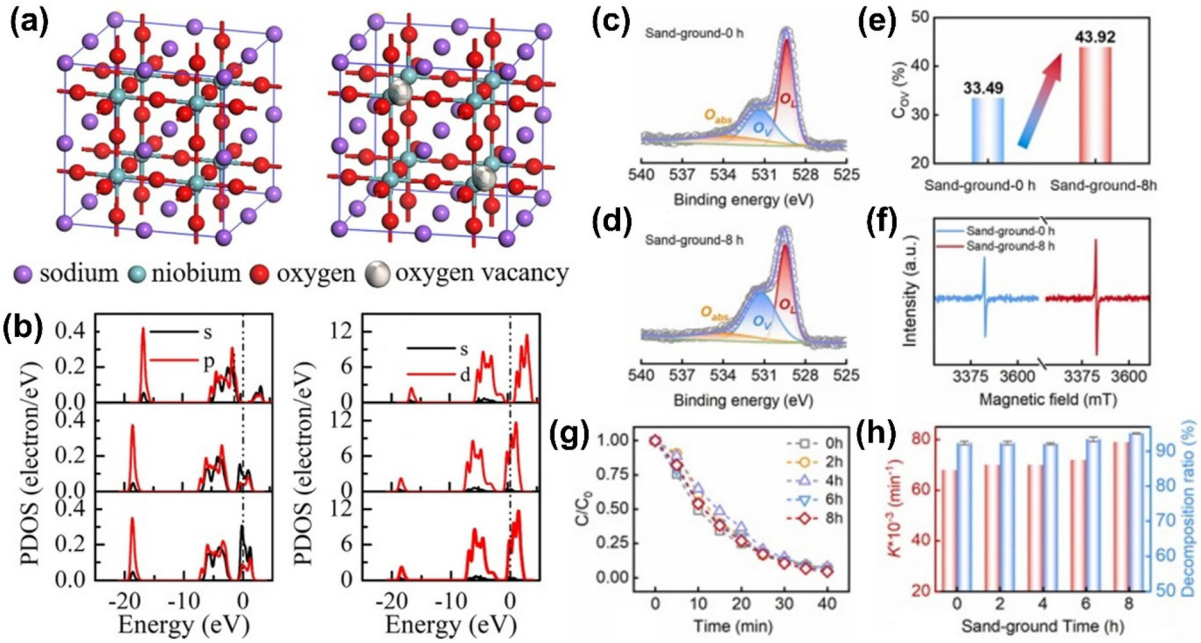

Fig. 6 (a and b) Crystal structures of primitive (left) and 5.6% oxygen vacancy containing $NaNbO_3$ (right). (b) PDOS of Na (left) and Nb atoms (right) in the $NaNbO_3$ with different oxygen vacancy concentrations of 0%, 2.8%, and 5.8% from top to bottom in each column, respectively. Reprinted with permission from ref. 100. Copyright 2023, Elsevier. (c–e) Comparison of (c and d) XPS spectra of O 1s, (e) concentration of oxygen vacancies, and (f) EPR spectra between KNN samples sand-grounded for 0 h and 8 h. (g) Piezocatalytic RhB degradation of KNN samples prepared using sand-ground at different durations and (h) corresponding reaction rate constant and decomposition rate. Reprinted with permission from ref. 102. Copyright 2023, Elsevier.

also promoted better adsorption of reactants such as oxygen and hydroxyl groups on the catalyst surface, generating more ROS for efficient dye degradation.

Finally, $KNbO_{3-x}$ samples with oxygen vacancies were prepared by reducing the $KNbO_3$ in a highly reducing environment using a reaction between Nb_2O_5 and KBH_4.[103] The introduction of oxygen vacancies slightly increased the charge carrier density, crucial for improving electron–hole pair separation and transport under mechanical stress. These vacancies also lowered the energy barrier for charge excitation, enabling more efficient electron migration into the conduction band, which resulted in improved hydrogen production rates under mechanical stress.

4.3. Morphology control

Morphology control is a powerful strategy for enhancing piezocatalytic and photo-piezocatalytic performance of materials. The structure and shape of piezoelectric materials significantly influence their ability to generate piezoelectric potential under mechanical stress, separate charge carriers, and provide active surface sites for catalytic reactions. In particular, controlling morphology at the nanoscale substantially increases the active surface area, which is crucial for improving catalytic efficiency. Nanostructuring into forms such as nanowires, nanorods, and nanosheets leads to higher surface-to-volume ratios, offering more active sites for reactant adsorption. For instance, 1D and 2D nanostructures like $ZnSnO_3$ nanowires and MoS_2 nanosheets have demonstrated superior piezocatalytic performance due to their large surface areas and efficient charge transport pathways.[17,104] Another key aspect of morphology control is the exposure of specific crystal facets. Different crystal planes possess distinct surface energies and catalytic activities, so tailoring the shape of piezocatalytic particles allows researchers to control the distribution of reactive sites. For instance, $Bi_4Ti_3O_{12}$ nanosheets synthesized *via* a molten-salt method exhibited exposed {001} facets, which were highly reactive for piezocatalytic applications.[105] The dimensionality of piezoelectric materials also directly affects their mechanical deformation ability and piezoelectric response. 2D layered materials, such as MoS_2 and $BiVO_4$, have shown excellent piezocatalytic behavior due to their ability to generate and maintain high piezoelectric potential when subjected to external mechanical forces.[106] The enhanced mechanical flexibility of 2D materials allows them to deform more easily under stress, thereby generating stronger piezoelectric potentials.

In KNN-based materials, Zhang *et al.* explored the effect of morphology control on the piezo- and photo-piezocatalytic performance of $KNbO_3$ by comparing nanosheets and nanocubes.[107] These two morphologies exhibited distinct catalytic behaviors (Fig. 7). $KNbO_3$ nanosheets showed significantly higher piezo- and photo-piezocatalytic efficiency than nanocubes. The larger surface area and superior mechanical flexibility of nanosheets enabled more efficient piezoelectric potential generation and better charge separation under mechanical

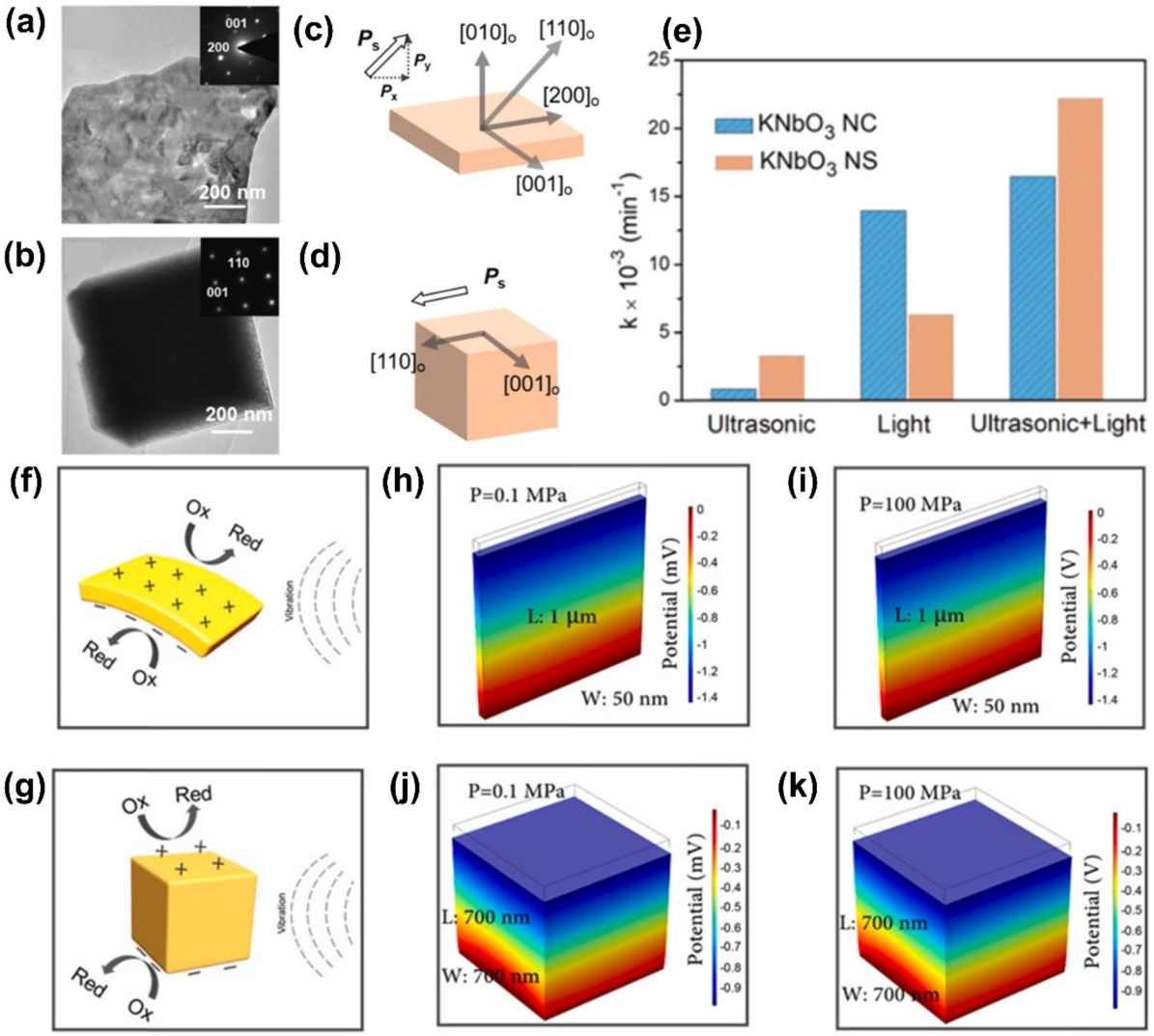

Fig. 7 (a and b) TEM images and (c and d) spontaneous polarization directions of $KNbO_3$ (a and c) nanosheet and (b and d) nanocube. (e) Reaction rate constants of RhB degradation for $KNbO_3$ nanosheet and nanocube under different stimuli. (f and g) Schematics showing the piezocatalytic mechanism of $KNbO_3$ (f) nanosheet and (g) nanocube. (h–k) Finite element method (FEM) simulation for the piezoelectric potential distribution in $KNbO_3$ (h and i) nanosheet and (j and k) nanocube at different cavitation pressures (0.1 MPa and 100 MPa). Reprinted with permission from ref. 107. Copyright 2019, Elsevier.

stress, leading to improved catalytic performance. The study also revealed that nanosheets had superior ferroelectric and piezoelectric responses relative to the nanocubes. The exposed crystal facets and polarization components in the nanosheets were more effective in promoting charge carrier separation under both light and mechanical excitation. Additionally, the polarization direction of the nanosheets, aligned along the [110] crystal direction, contributed to better catalytic efficiency than nanocubes, which had only a single polarization component.

4.4. Heterojunction formation

Heterojunction formation is one of the most effective strategies for enhancing piezocatalytic and photo-piezocatalytic activities, as single-component materials often face limitations in terms of charge separation and catalytic efficiency. By combining two or more materials with different electronic structures, heterojunctions create an interface that facilitates efficient charge transfer. The band alignment between the materials in the heterojunction is crucial, as it determines the movement of electrons and holes, significantly boosting catalytic performance. Ferroelectric piezocatalysts often have low charge carrier concentrations, while semiconductor-based photocatalysts experience severe recombination of photogenerated electron–hole pairs.[4,51] To overcome these limitations, heterostructures or nanocomposites have been widely explored, especially in photo-piezocatalysis, since Wang *et al.* introduced the concept of piezo-phototronics in 2010.[23,108,109] The additional piezoelectric potential generated under mechanical stress, along with the built-in electric field at the

heterojunction interface, can further enhance charge separation and migration in these systems.[110] The piezoelectric potential can also reduce the barrier height, tilt energy bands, shift heterojunctions from type-II to S-scheme, adjust Fermi energy levels, and strengthen the interfacial electric field.[90,111–114] These effects will be explored in more detail below.

Several types of heterojunctions are commonly employed in piezocatalytic and photo-piezocatalytic systems, including Type-I, Type-II, and S-scheme heterojunctions, each with distinct mechanisms for improving charge separation and catalytic performance.[115]

Type-I heterojunctions. In a type-I heterojunction, the conduction band (CB) and the valence band (VB) of one material are positioned within the corresponding bands of the other material.[116] Although this alignment limits charge separation, piezoelectric potential-driven band titling can overcome this limitation by directing electrons and holes in opposite directions. For instance, a Type-I heterojunction between n-type $KNbO_3$ and n-type Ag_2O ($KNbO_3$@Ag_2O) was shown to enhance the piezocatalytic degradation of Orange II.[117] The piezoelectric potential generated in $KNbO_3$ under mechanical vibration tilted the energy bands, aligning the CB and VB levels of Ag_2O and $KNbO_3$ closer on the positive and negative side, respectively, promoting charge separation and facilitating redox reactions on the catalyst surface. A similar example is the 1D of $KNbO_3$/2D MoS_2 heterostructure, where the combination of heterojunction formation and flexible morphologies improved photo-piezocatalytic hydrogen production (Fig. 8(a) and (b)).[27] Under light illumination, photo-induced electrons and holes were generated in both $KNbO_3$ and MoS_2. The spontaneous polarization-induced band bending in ferroelectric $KNbO_3$ drove charge carriers in opposite directions, reducing recombination. Additionally, the piezoelectric potential generated by ultrasonic vibration further bent the energy bands, facilitating the transfer of photogenerated electrons and holes (Fig. 8(c)).

Piezoelectric potential-driven band tilting can also be used to overcome limitations in redox reactions due to unfavorable band edge positions. For instance, in the Type-I heterojunction between $NaNbO_3$ and MoS_2, where both the CB and VB of MoS_2 are positioned between those of $NaNbO_3$, redox reactions for generating ROS primarily occur through the electrons and holes from MoS_2 (Fig. 8(d)).[90] The VB edge position of MoS_2, being more negative than the redox potential of $^{\bullet}OH/H_2O$, makes generating $^{\bullet}OH$ radicals thermodynamically unfeasible. However, the piezoelectric potential generated under ultrasonic vibration allows $NaNbO_3$ to act as a self-powered parallel capacitor, providing an electric field to MoS_2 attached to $NaNbO_3$. This creates a positive and negative bias at different sides of MoS_2, shifting the Fermi energy levels downward and upward, respectively (Fig. 8(e)). In this piezo-electrocatalytic system, the generation of $^{\bullet}OH$ radicals becomes feasible at the positively biased MoS_2 side due to the favorable VB edge position.

Type II heterojunctions. Type-II heterojunctions, where the CB of one material is lower than that of the other, and the VB of the second material is higher, are widely used in catalytic applications. This band alignment allows for the spatial separation of electrons and holes, reducing recombination, which

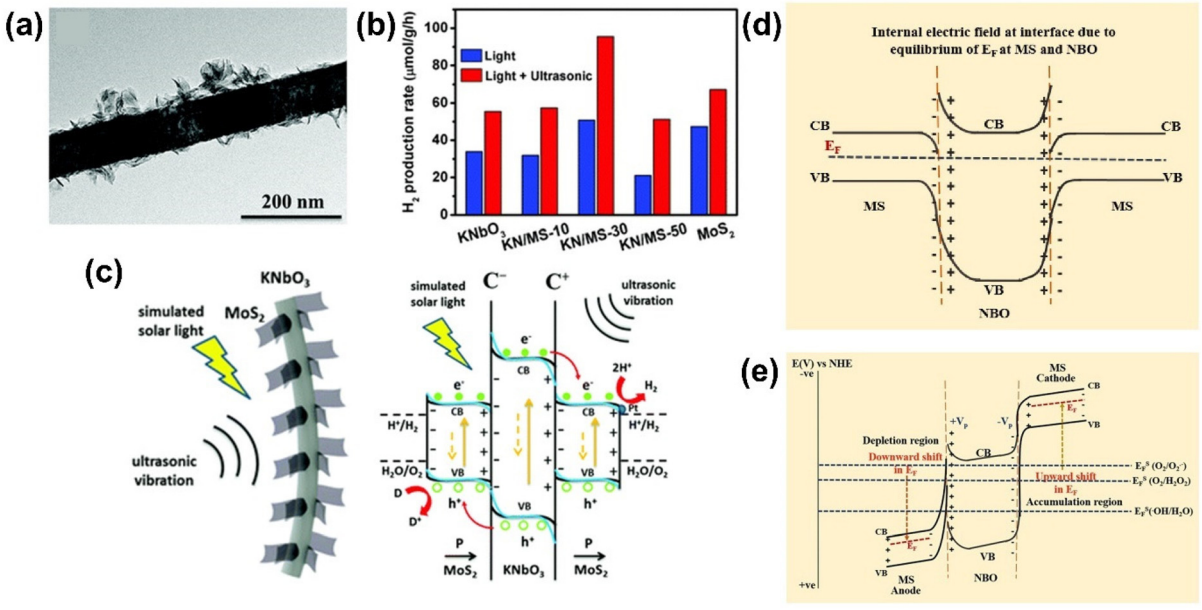

Fig. 8 (a) Representative TEM image of 30 wt% MoS_2 nanosheets attached $KNbO_3$ nanowire (KN/MS-30) and (b) H_2 production rates of $KaNbO_3$, MOS_2 and their heterostructures under different external stimuli. (c) Schematic illustration showing photo-piezocatalytic mechanism of $KNbO_3$/MoS_2 heterostructure. Reprinted with permission from ref. 27. Copyright 2019, Royal Society of Chemistry. (d and e) Energy band structures of $NaNbO_3$/MoS_2 heterostructure (d) in equilibrium and (e) under ultrasonic vibration. Reprinted with permission from ref. 90. Copyright 2023, Elsevier.

makes Type-II heterojunctions highly effective in both piezocatalysis and photo-piezocatalysis.[118] However, one drawback of the Type-II heterojunctions is the potential decrease in redox activity due to the mutual repulsion between charge carriers. Several Type-II heterostructures, including $BaTiO_3/KNbO_3$, $KNbO_3/ZnO$, $NaNbO_3/g\text{-}C_3N_4$ have demonstrated superior photo-piezocatalytic degradation of organic pollutants by promoting charge separation and reducing recombination.[119–121]

Recently, a $KNbO_3/WO_3$ Type-II heterojunction was fabricated, exhibiting enhanced photo-piezocatalytic activity due to the synergistic effects of the Type-II heterojunction and strong polarization-induced electric field in $KNbO_3$ (Fig. 9(a)–(d)).[122] However, this static polarization field in $KNbO_3$ can be screened by free charges in the solution, reducing photocatalytic efficiency. Applying periodic ultrasound vibration can generate an alternating polarization electric field, promoting catalytic activity (Fig. 9(e)).

As observed in Type-I heterojunctions, the piezoelectric potential can shift the band edge position and Fermi energy level, enabling redox reactions that are otherwise thermodynamically unfavorable. For example, in an n-type KNN/p-type CuO Type-II heterostructure, a p–n junction was formed by matching their Fermi energy levels at static equilibrium (Fig. 9(f)).[4] Under light illumination, photo-excited electrons moved to the CB of KNN, whereas holes migrated to the VB of CuO (Fig. 9(g)). However, the VB edge of CuO near the positively polarized KNN became more positive than the redox potential of $OH^-/{}^{\bullet}OH$, resulting in low catalytic efficiency for RhB degradation. Applying a strong piezoelectric potential (~3.5 V), generated by ultrasonication in single-crystal ferroelectric KNN, induced a linear shift in the Fermi level of KNN, altering the energy levels of CuO attached to the opposing polarization sides of KNN by an amount equivalent to the piezoelectric potential. As a result, the VB edge of CuO near the positively polarized KNN became more positive than the redox potential of $OH^-/{}^{\bullet}OH$, promoting hole transfer from CuO to water molecules and generating $^{\bullet}OH$ radicals (Fig. 9(h)). The combined effects of light and ultrasound waves led to higher photo-piezocatalytic activity than the sum of the individual photocatalytic and piezocatalytic performances (Fig. 9(i)). This improvement was due to the increased carrier concentration and enhanced electron–hole separation efficiency, driven by the photo-piezo coupling effect and heterojunction formation.

S-scheme heterojunctions. S-scheme heterojunctions have emerged as a promising approach for enhancing photocatalytic and piezocatalytic performance.[116] Unlike traditional Type-I and Type-II heterojunctions, S-scheme heterojunctions exhibit a unique band alignment that facilitates efficient charge separation and reduces recombination. In an S-scheme heterojunction, the CB of one material aligns with the VB of the other material, where the Fermi levels of the two materials are aligned, but the bandgaps overlap. This type of band alignment promotes efficient charge separation, as electrons from the CB of one material can directly recombine with holes in the VB of the other material. This recombination process effectively removes low-energy charge carriers, leaving behind high-energy electrons and holes for catalytic reactions. While S-scheme heterojunctions offer significant promise, challenges remain in creating stable and efficient systems with suitable materials.

S-scheme heterojunctions are conceptually similar to direct Z-scheme heterojunctions, as both mechanisms selectively recombine low-energy carriers while retaining high-energy electrons and holes for catalytic reactions.[123] The key distinction lies in the emphasis on a built-in electric field in S-scheme systems, which enhances charge separation by spatially separating high-energy carriers.[124] In contrast, direct Z-scheme heterojunctions rely on a straightforward charge migration pathway without explicitly leveraging an electric field. Both approaches eliminate the need for mediators, unlike indirect Z-schemes, which depend on redox pairs or conductors and can introduce recombination losses and complexity.[125] Based on the S-/direct Z-scheme principles, double or triple S-/Z-scheme heterojunctions can be created by combining multiple semiconductors to further enhance charge separation.[126] These advanced systems leverage the complementary properties of their components to achieve superior catalytic efficiency. However, constructing such complex heterojunctions poses significant challenges, including ensuring interfacial stability and precise alignment of the electronic structures. Despite their potential, multiple heterojunction systems remain underexplored in piezocatalysis and photo-piezocatalysis compared to single S-scheme and direct Z-scheme systems. Further research is needed to address these challenges and unlock their full potential for practical applications.

For S-scheme systems, a recent study explored the formation of $NaNbO_3/BiVO_4$ S-scheme heterostructures using a two-step hydrothermal synthesis (Fig. 10(a) and (b)).[127] Based on the band structures of $NaNbO_3$ and $BiVO_4$, both Type-II and S-scheme heterojunctions were possible. In the Type-II mechanism, electrons move to the CB of $BiNO_4$ and holes migrate to the VB of $NaNbO_3$, in which the VB of $NaNbO_3$ (2.64 eV *vs.* NHE) could produce $^{\bullet}OH$ radicals ($H_2O/{}^{\bullet}OH$ = 2.40 eV *vs.* NHE), while the CB of $BiNO_4$ (0.51 eV *vs.* NHE) is not favorable to generate $^{\bullet}O_2^-$ radical ($O_2/{}^{\bullet}O_2^-$ = −0.33 eV *vs.* NHE). On the other hand, in the S-scheme heterojunction, electrons in $BiVO_4$ transfer to $NaNbO_3$ and rapidly recombine with holes in the VB of $NaNbO_3$. This leaves behind high-energy electrons and holes in the $NaNbO_3$ and $BiVO_4$, respectively. In this scenario, the electrons from $NaNbO_3$ and the holes from $BiVO_4$ are more negative and positive than the $O_2/{}^{\bullet}O_2^-$ and $H_2O/{}^{\bullet}OH$, respectively, producing a large number of ROS. XPS analysis confirmed the electron transfer from $BiVO_4$ to $NaNbO_3$ (Fig. 10(c) and (d)) and scavenging tests revealed the presence of $^{\bullet}OH$ and h^+ radicals as active species for the photo-piezocatalytic tetracycline removal. These results further support the S-scheme charge transfer mechanism as the dominant mechanism in this system (Fig. 10(e)).

Kumar *et al.* recently demonstrated an interesting conversion from a Type-II to an S-scheme heterojunction in $NaNbO_3/$

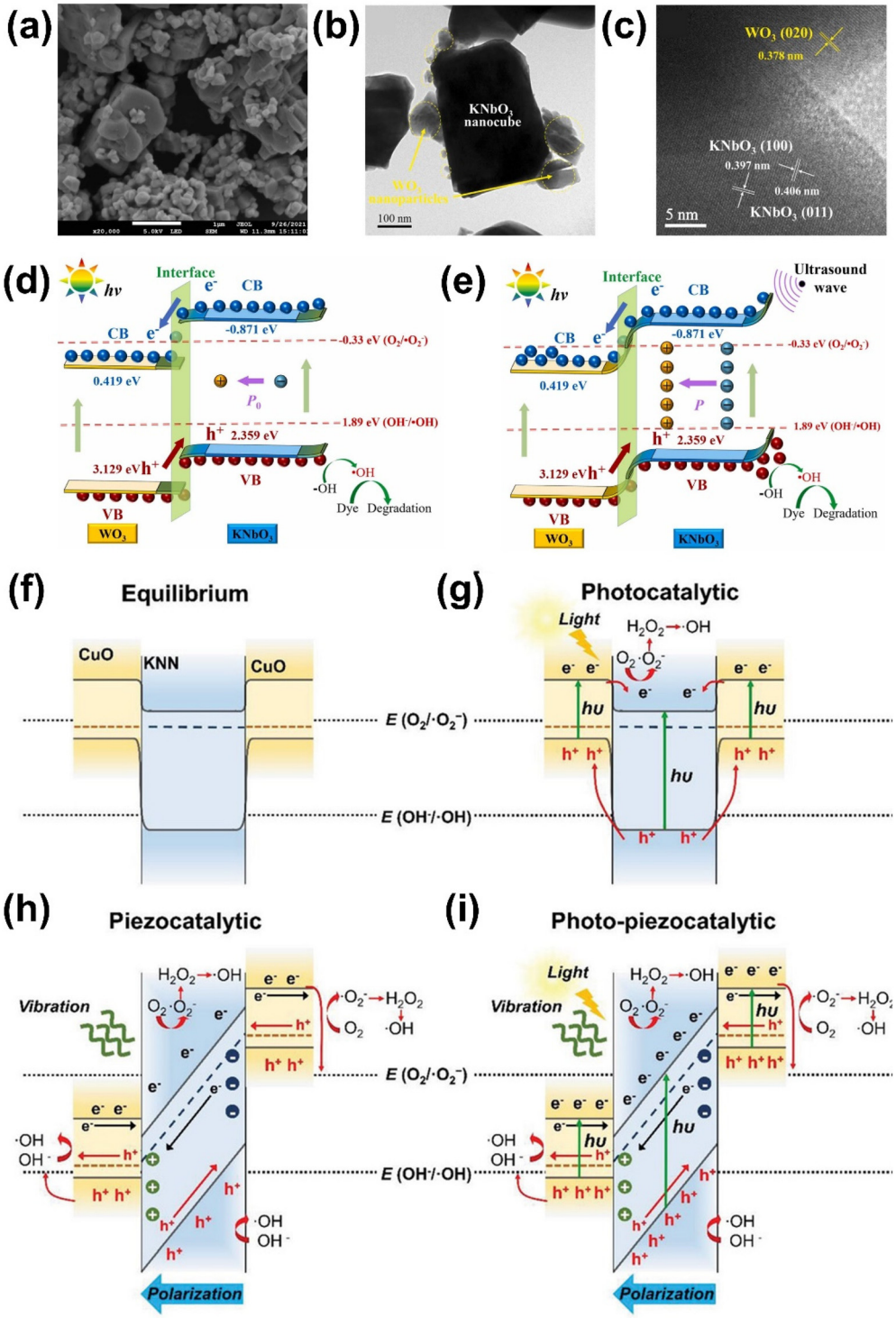

Fig. 9 (a) SEM, (b) TEM, and (c) HR-TEM images of 50%$KNbO_3/WO_3$ heterostructure. (d and e) Schematic illustrations showing (d) photocatalytic and (e) photo-piezocatalytic dye degradation mechanisms of $KNbO_3/WO_3$ heterostructure. Reprinted with permission from ref. 122. Copyright 2023, Elsevier. (f–i) Schematics showing energy band structure of KNN/CuO (f) in equilibrium, (g) under light irradiation alone, (h) under ultrasonication alone, and (i) under both light illumination and ultrasonication. Reprinted with permission from ref. 4. Copyright 2024, Wiley.

g-C_3N_4 systems, driven by the piezoelectric potential generated by ultrasonic vibration.[128] In the absence of ultrasonication, the transfer of electrons and holes follows the typical Type-II heterojunction mechanism of the $NaNbO_3$/g-C_3N_4 system (Fig. 10(f)). Scavenging tests revealed that $^{\bullet}OH$ played a major role, followed by holes and $^{\bullet}O_2^-$ in the piezocatalytic degra-

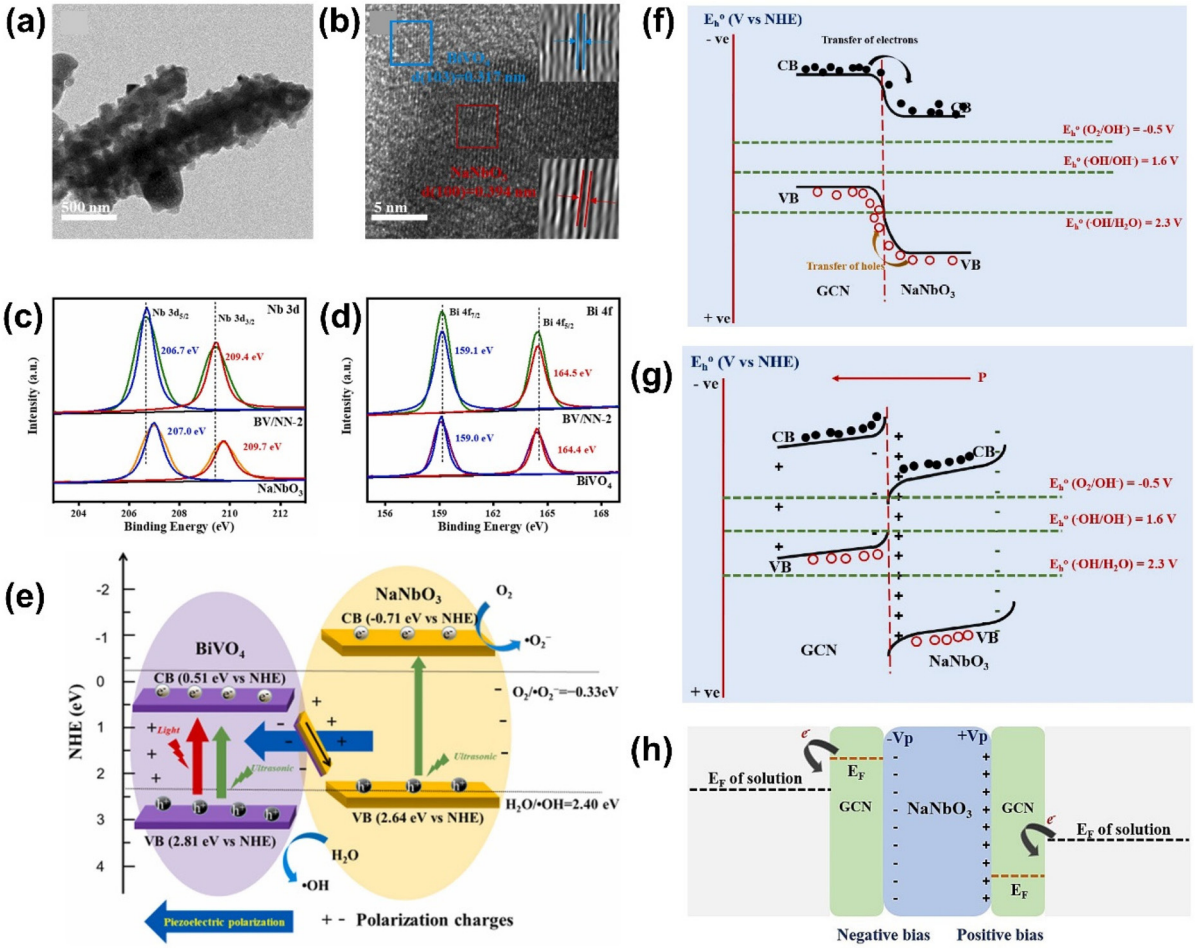

Fig. 10 (a) TEM and (b) HR-TEM images of $NaNbO_3/BiVO_4$ heterostructures. (c and d) XPS spectra of (c) Nb and (d) Bi of $NaNbO_3$, $BiVO_4$, and $NaNbO_3/BiVO_4$. (e) Schematic drawing of S-scheme heterojunction between $NaNbO_3$ and $BiVO_4$. Reprinted with permission from ref. 127. Copyright 2023, Elsevier. (f and g) Schematic illustrations of (f) Type-II and (g) S-scheme heterojunctions of $NaNbO_3/g\text{-}C_3N_4$ system. (h) The formation of the piezo-electrocatalytic system in $NaNbO_3/g\text{-}C_3N_4$ heterojunction. Reprinted with permission from ref. 128. Copyright 2023, Elsevier.

dation of metronidazole (MET). However, the VB of $g\text{-}C_3N_4$ has insufficient redox potential compared to the $H_2O/^{\bullet}OH$ redox couple, which does not fully explain the observed improvement in MET removal efficiency with the Type-II $NaNbO_3/g\text{-}C_3N_4$ system. Upon ultrasonication, the piezoelectric potential caused a reduction and increase in potential at the positively and negatively charged surfaces, respectively, compared to the bulk, leading to downward and upward band tilting. This band tilting resulted in the formation of an S-scheme heterojunction, which improved charge separation during mechanical excitation (Fig. 10(g)). Additionally, the positive and negative piezoelectric potentials generated in $NaNbO_3$ created positive and negative biases in $g\text{-}C_3N_4$, shifting the Fermi energy levels downward and upward, respectively (Fig. 10(h)). The S-scheme heterojunction was thus established between the positively charged side of $NaNbO_3$ and the negatively charged side of $g\text{-}C_3N_4$, allowing holes in the VB of $NaNbO_3$ to participate in the generation of $^{\bullet}OH$ through the oxidation of H_2O, as well as the direct oxidation of MET.

Heterojunctions, including Type-I, Type-II, and S-scheme (direct Z-scheme) configurations, play pivotal roles in enhancing catalytic efficiency by improving charge separation and redox potential. Type-I heterojunctions have limited charge separation capability, but this limitation can be mitigated by piezoelectric potential, which tilts energy bands. Type-II heterojunctions improve spatial charge separation but may reduce redox efficiency due to energy loss during charge transfer. Direct Z-scheme and S-scheme heterojunctions address these issues by selectively recombining low-energy carriers while retaining high-energy electrons and holes for redox reactions. However, they face challenges such as material limitations and complex design requirements, which can hinder scalability. In broader applications, such as environmental remediation or energy conversion, simpler configurations like Type-II heterojunctions may offer comparable performance due to easier fabrication and greater material flexibility. Optimizing these heterojunctions for specific applications remains an important research direction.

4.5. Metal deposition/loading

Metal deposition or loading can effectively enhance the piezocatalytic and photo-piezocatalytic activities of ferroelectric materials.[50] By introducing noble metals like gold, silver, and platinum onto the surface of piezoelectric catalysts, several beneficial effects are achieved, including enhanced light absorption, improved charge separation, and increased catalytic activity.[129] These effects are primarily driven by the localized surface plasmon resonance (LSPR) effect of the metal nanoparticles, the formation of Schottky barriers at the metal-catalyst interfaces, and their synergistic interaction with the piezoelectric properties of the catalyst. LSPR occurs when electromagnetic radiation interacts with metal nanoparticles, causing collective oscillation of free electrons at the nanoparticle surface. This resonance with incident light significantly enhances light scattering, absorption, and field localization near the nanoparticle surface.[130]

In non-KNN materials, Au nanoparticles deposited onto $AgNbO_3$ cubes significantly improved photo-piezocatalytic activity by leveraging the LSPR effect to generate high-energy hot electrons under visible light.[131] These electrons overcame the Schottky barrier and transferred into the conduction band (CB) of $AgNbO_3$, driving the reduction reactions. Simultaneously, the piezoelectric potential generated in $AgNbO_3$ under mechanical stress enhanced charge separation and minimized recombination, further boosting catalytic efficiency. Similarly, Pt nanoparticles deposited on $BaTiO_3$ improved catalytic performance through plasmonic effects combined with piezoelectric field-induced charge separation, demonstrating the potential of metal deposition in non-KNN systems.[132]

In KNN-related systems, notable progress has also been achieved in photo-piezocatalysis. For example, Ag dots were decorated on $NaNbO_3$ ($Ag/NaNbO_3$) particles, which were prepared by a solid-state reaction (for $NaNbO_3$) followed by a photo-reduction method for Ag dot decoration (Fig. 11).[133] The deposition of Ag nanoparticles enhanced the photocatalytic activity of $Ag/NaNbO_3$ by narrowing the bandgap and extending light absorption into the visible range. The Schottky barrier between Ag and $NaNbO_3$ facilitated charge separation by allowing photogenerated electrons in $NaNbO_3$ to transfer to Ag, where they were trapped, preventing recombination. Additionally, the plasmonic excitation of Ag under visible light generated hot electrons, which were transferred to the CB of $NaNbO_3$, further boosting the piezo-photocatalytic degradation of organic pollutants like RhB and antibiotics such as ciprofloxacin and tetracycline. The combined piezoelectric and plasmonic effects in the $Ag/NaNbO_3$ system led to enhanced ROS generation, making it highly efficient for environmental remediation.

In addition to photo-piezocatalysis, this approach has been demonstrated as an effective way in KNN-based photocatalysis. Au nanoparticles supported on $KNbO_3$ microcubes exhibited enhanced photocatalytic performance for hydrogen peroxide (H_2O_2) decomposition and methylene blue degradation under visible light.[134] The improvement is attributed to LSPR effects and efficient charge transfer at the $Au/KNbO_3$ interface, which promotes the generation of highly reactive hydroxyl radicals. Additionally, Pt nanoparticles on $NaNbO_3$ nanowires showed an 8.3-fold increase in hydrogen evolution efficiency compared to pristine $NaNbO_3$, due to the superior dispersion of Pt nanoparticles and enhanced electron–hole separation facilitated by the one-dimensional nanowire structure.[135]

Despite these advances, research on metal deposition for KNN-based systems remains limited, especially in photo-piezocatalysis. Expanding studies in this area could unlock new opportunities for leveraging metal-induced LSPR effects and piezoelectric potentials to further enhance catalytic performance. Overall, metal deposition/loading plays a critical role in improving the efficiency of piezocatalytic and photo-piezocatalytic systems. The combination of metal-induced LSPR and piezoelectric effects leads to more efficient charge separation, greater ROS generation, and enhanced light absorption, making metal-loaded piezoelectric materials highly effective for applications such as environmental purification and energy conversion.

4.6. Modulation of external conditions for enhancing piezo- and photo-piezocatalysis

In piezocatalysis and photo-catalysis, optimizing external conditions is essential for improving catalytic efficiency. Two key approaches such as poling and resonance frequency matching can significantly boost the generation of piezoelectric potentials and enhance charge carrier separation during catalytic processes.[136] By strategically applying these techniques, the piezoelectric response of materials can be amplified, leading to higher catalytic performance, particularly in environmental and energy applications.

Poling treatment. It involves applying an external electric field to align the internal dipoles of piezoelectric materials, creating a macroscopic polarization.[137] This alignment enhances the piezoelectric potential generated when mechanical stress is applied, resulting in improved charge separation and catalytic performance. For instance, in $K_{0.5}Na_{0.5}NbO_3$–$Bi_{0.5}Na_{0.5}ZrO_3$ (KNN–BNZ) ceramics, poling treatment significantly enhanced the piezocatalytic degradation of organic pollutants such as Rhodamine B (RhB), methylene blue (MB), and amino black 10B (AB10B) (Fig. 12(a) and (b)).[138] The poling process aligned the electric domains, facilitating better charge separation and promoting the generation of ROS. Poled KNN–BNZ ceramics exhibited a reaction rate constant (k) that was 3.44-fold higher than unpoled samples during RhB degradation. Additionally, the poling-induced phase transformation from higher symmetry to lower symmetry orthorhombic phases enhanced the piezoelectric response, further boosting catalytic performance. Similarly, the poling treatment of ferroelectric $K_{0.5}Na_{0.5}NbO_3$ (KNN) particles showed a marked increase in piezo-photocatalytic performance.[139] Poled KNN samples achieved significantly higher dye degradation efficiency (92% for RhB) compared to unpoled samples, primarily due to the enhanced internal electric fields that pro-

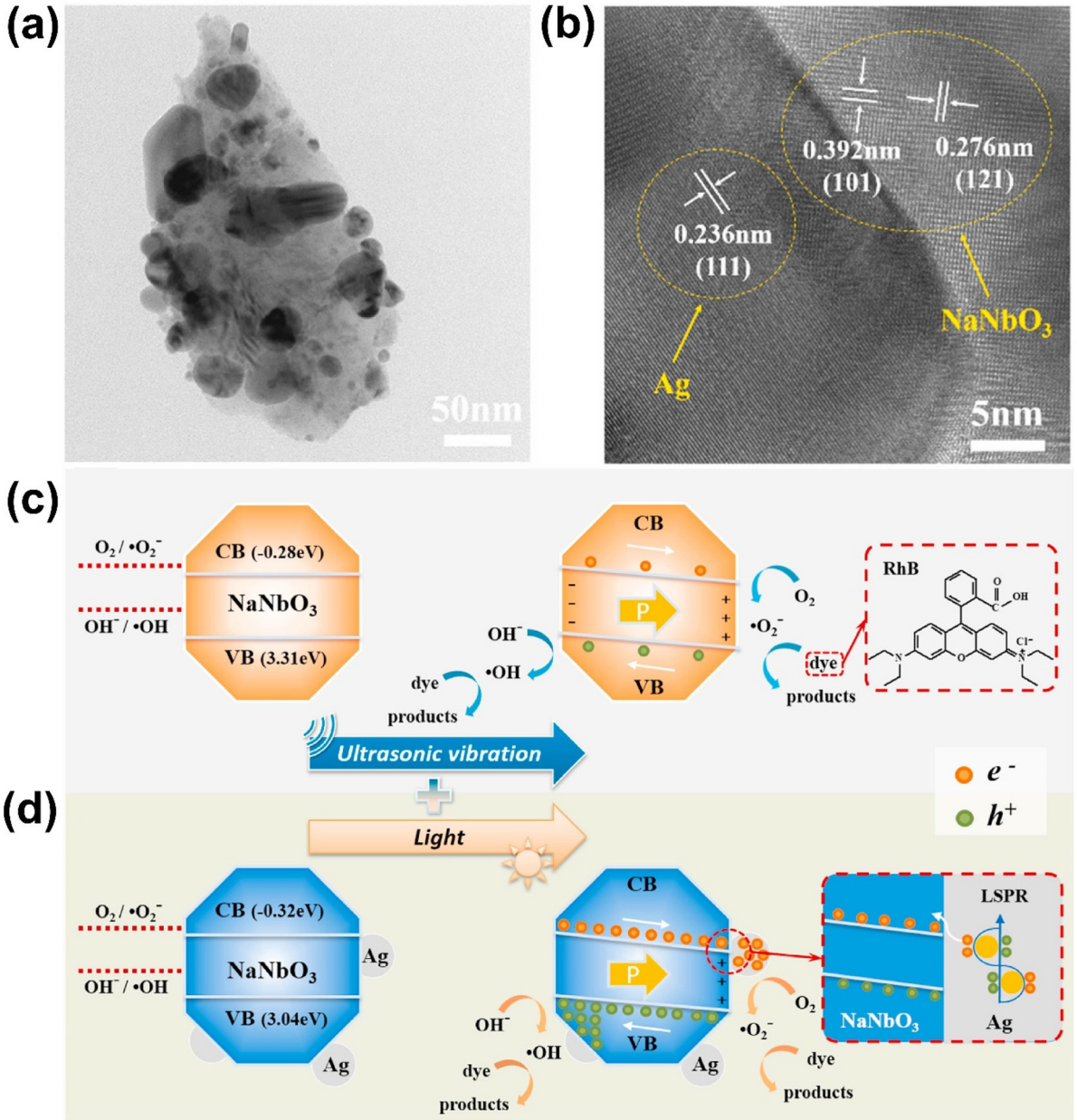

Fig. 11 (a) TEM and (b) HR-TEM images of Ag dot decorated $NaNbO_3$. (c and d) Possible mechanism of piezocatalytic and photo-piezocatalytic dye degradation of Ag/$NaNbO_3$. Reprinted with permission from ref. 133. Copyright 2022, Elsevier.

moted more efficient charge carrier migration. Electrochemical impedance spectroscopy (EIS) confirmed that poled samples had lower charge transfer resistance and higher charge separation efficiency, resulting in superior bi-catalytic performance under simultaneous ultrasonication and light irradiation.

Resonance frequency matching. Every piezoelectric material has a specific resonance frequency at which it undergoes maximum mechanical deformation under applied vibrations. By matching the applied ultrasound frequency to the material's natural resonance frequency, the piezoelectric potential generated under mechanical stress can be maximized, thereby enhancing catalytic performance. A study on $KNbO_3$ nanofibers demonstrated the importance of resonance frequency in enhancing piezocatalytic degradation of RhB under low-frequency ultrasound (LFUS).[140] When the applied ultrasound frequency matched the resonance frequency of the $KNbO_3$ nanofibers (30 kHz), the material exhibited maximum deformation and generated the highest piezoelectric potential (Fig. 12(c)). This resonance-induced amplification of the piezoelectric potential led to a 4.4-fold increase in degradation efficiency compared to off-resonance conditions (20 kHz and 40 kHz). The study showed that resonance frequency matching not only enhanced charge separation but also allowed for high

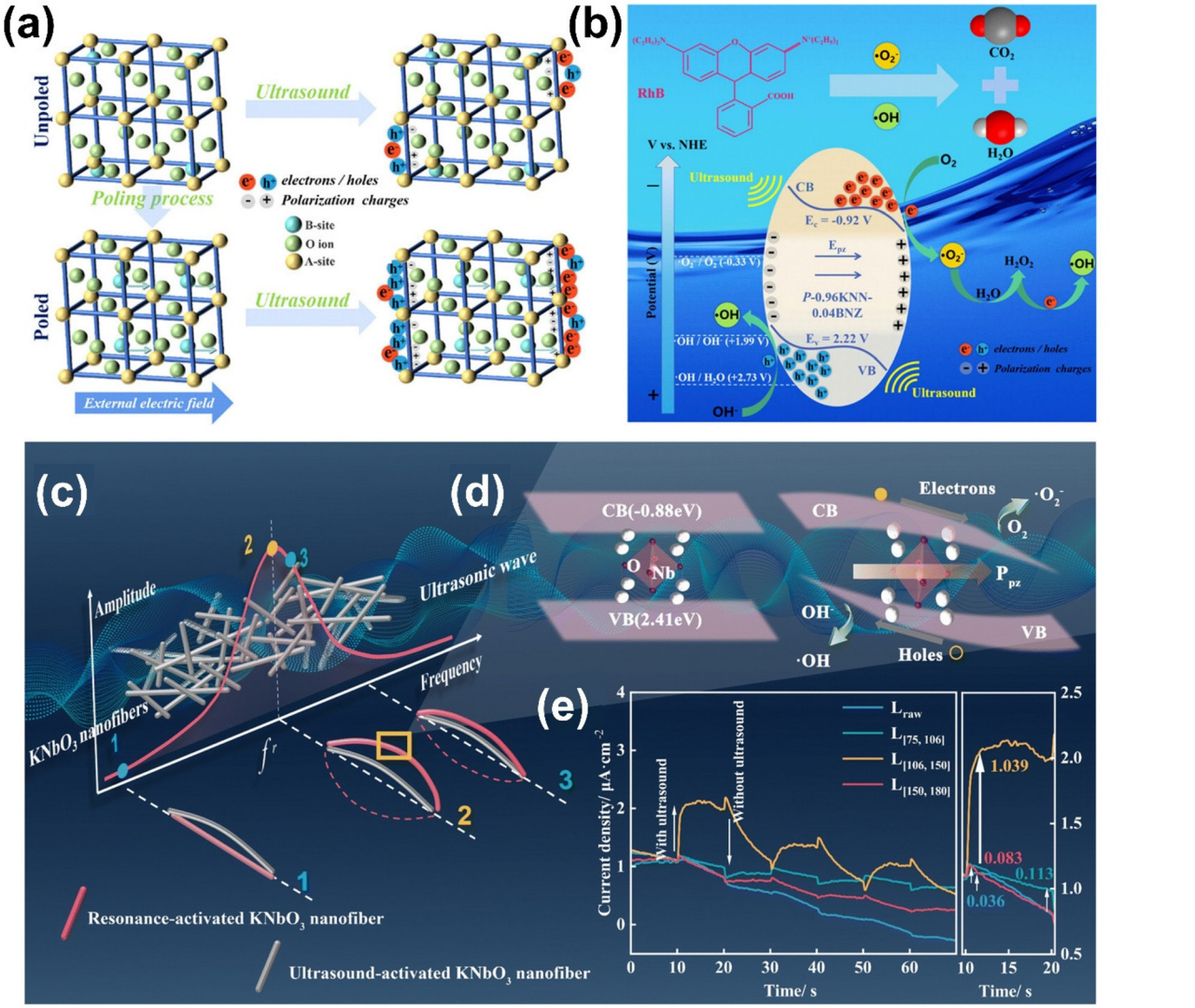

Fig. 12 (a) Schematic drawings of poling and ultrasound actions on KNN-BNZ ceramics. (b) A possible mechanism of piezocatalytic dye degradation using polarized KNN-BNZ ceramics. Reprinted with permission from ref. 138. Copyright 2024, Wiley. (c) Resonance-induced deformation and (d) band structure variation of $KNbO_3$. (e) Current density of $KNbO_3$ with different natural frequencies at 30 kHz. Reprinted with permission from ref. 140. Copyright 2024, Royal Society of Chemistry.

catalytic efficiency at lower ultrasound power levels, making it an energy-efficient strategy. Under resonance conditions, ROS like hydroxyl radicals and superoxide radicals were efficiently produced, leading to more effective degradation of RhB (Fig. 12(d) and (e)).

5. Applications of KNN-based piezo- and photo-piezocatalysts

Piezocatalysis and photo-piezocatalysis offer promising solutions for addressing various environmental and energy-related challenges by converting mechanical energy and light into chemical energy. The use of piezoelectric materials in these catalytic processes has led to significant advancements, particularly in the degradation of organic pollutants.[141] Recently, the scope of applications for these materials has expanded to include hydrogen evolution reactions (HER), oxygen evolution reactions (OER), CO_2 reduction, and nitrogen fixation. Below, we explore these applications, focusing on the latest research findings on KNN-based materials.

5.1. Degradation of organic pollutants

Organic pollutants such as industrial dyes, pharmaceuticals, and agricultural chemicals pose a major threat to the environment.[142] Piezocatalysis and photo-piezocatalysis have emerged as effective techniques for degrading these pollutants by generating ROS under mechanical stress and light exposure. The mechanisms underlying piezocatalysis and photo-piezocatalysis involve a synergistic interplay between the piezoelectric

effect and advanced oxidation processes (AOPs). Under mechanical stress and/or light exposure, free electrons and holes are generated within the material, migrate to its surface, and participate in redox reactions that degrade pollutants. These processes lead to the formation of ROS, which are crucial in breaking down organic molecules into harmless products. Sulfate radical-based AOPs, involving persulfate ($S_2O_8^{2-}$) and peroxymonosulfate (HSO_5^-), are particularly effective due to their high oxygen reduction potential, wide pH range, and long half-life.[143,144] Examples of ROS-driven reactions include:

$$e_{CB}^- + O_2 \rightarrow {}^{\bullet}O_2^-$$

$${}^{\bullet}O_2^- + e_{CB}^- + 2H^+ \rightarrow H_2O_2$$

$$H_2O_2 \rightarrow {}^{\bullet}OH + {}^{\bullet}OH$$

$$h_{VB}^+ + OH^- \rightarrow {}^{\bullet}OH$$

$$h_{VB}^+ + H_2O \rightarrow H^+ + {}^{\bullet}OH$$

$$HSO_5^- + e_{CB}^- \rightarrow {}^{\bullet}SO_4^{2-} + OH$$

$$S_2O_8^{2-} + {}^{\bullet}SO_4^- \rightarrow SO_4^{2-} + {}^{\bullet}S_2O_8^-$$

$$SO_5^{2-} + SO_5^{2-} \rightarrow 2SO_4^{2-} + {}^1O_2$$

$$\text{Organic molecules} + \text{ROS} \rightarrow \text{harmless products}$$

These radicals attack pollutants, breaking them into smaller fragments and mineralizing them into CO_2 and H_2O.

A recent study demonstrated the superior performance of KNN ferroelectrics in degrading organic dyes such as RhB and MO under ultrasonic vibration.[145] Three different KNN piezocatalysts were prepared: KNN powder calcinated at 850 °C (KNN-1), KNN powder sintered at 1070 °C (KNN-2), and KNN piezoceramics sintered at 1070 °C (KNN-3) (Fig. 13(a)). Among these, the KNN-3 sample exhibited the highest catalytic activity for RhB degradation, with a reaction rate constant 2.08- and 1.37-fold higher than KNN-1 and KNN-2, respectively. This enhanced performance of KNN-3 was attributed to its superior polarization intensity, increased oxygen vacancies, and higher charge carrier concentrations, which promoted better charge separation and ROS generation. Additionally, the KNN-3 sample exhibited excellent inhibitory effects on *Staphylococcus aureus* and *Escherichia coli* strains.

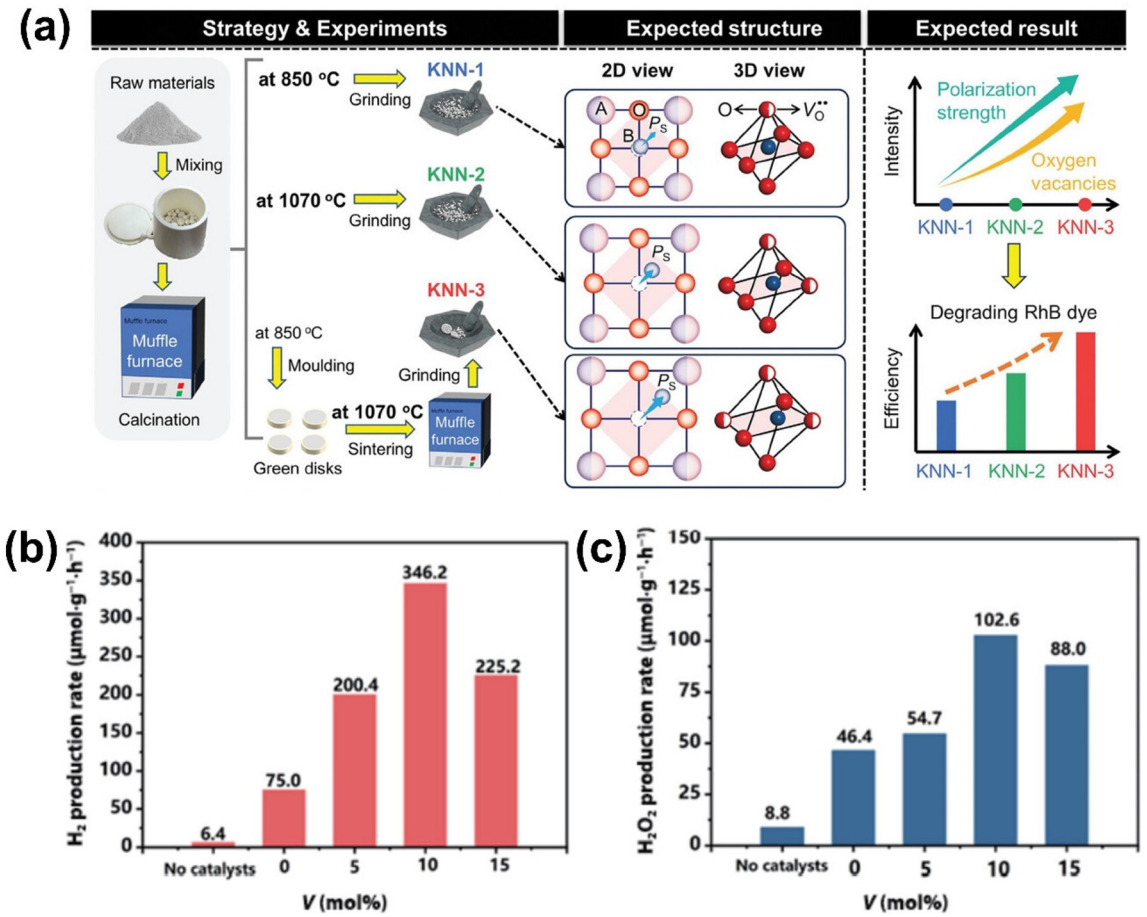

Fig. 13 (a) Schematics on experimental procedures, expected structures, and properties of three different KNN materials prepared by applying different calcination and sintering conditions. Reprinted with permission from ref. 145. Copyright 2024, Wiley. (b) Piezocatalytic H_2 and (c) H_2O_2 production rates of V-doped $NaNbO_3$ samples with different V doping. Reprinted with permission from ref. 150. Copyright 2022, Springer.

The elemental doing approach has been proven to improve the photo-piezocatalytic activity of $NaNbO_3$ for RhB degradation.[146] The introduction of La, Mn, and Ni into $NaNbO_3$ lattice ($0.1La(Mn_{0.5}, Ni_{0.5})O_3$–$0.9NaNbO_3$; (0.1LMN)) reduced the bandgap from 3.40 eV to 2.60 eV, enabling better utilization of visible light. Simultaneously, the doping increased lattice distortion, which improved piezoelectric properties and facilitated the separation and migration of photogenerated charge carriers. Under the synergistic effect of light irradiation and ultrasonic vibration, 0.1LMN achieved a degradation rate of 89.7% within 100 min, with a reaction rate constant (k) of 0.022 min^{-1}, which was 2.44-fold higher than of pristine $NaNbO_3$.

Numerous innovative studies have explored the use of KNN-based materials in degrading organic pollutants through piezocatalysis and photo-piezocatalysis, which are summarized in Table 1.

5.2. Hydrogen production

The hydrogen evolution reaction (HER) is a critical process in water splitting, enabling the production of hydrogen (H_2), a

Table 1 Summary of degradation of organic pollutants using KNN-based materials

Materials	Pollutant	Catalysis type	Reaction condition (U^*, L^*)	k^* (min^{-1})/E^*(%)	Ref.
$K_{0.5}Na_{0.5}NbO_3$	RhB	Piezocatalysis	U: 180 W, 40 kHz	0.0198/95.7 (in 160 min)	165
$NaNbO_3$	RhB	Piezocatalysis	U: 40 kHz	0.00937/75.8 (in 160 min)	166
Li doped $K_{0.5}Na_{0.5}NbO_3$	RhB	Piezocatalysis	U: 300 W, 40 kHz	0.025/91 (in 100 min)	8
$KNbO_3$ nanosheet, nanocube	RhB	Photo-Piezocatalysis	U: 110 W, 40 kHz L: 300 W (Xe)	Nanosheet = 0.022/92.6 Nanocube = 0.016	107
$BaTiO_3/KNbO_3$ composites	DLB5B	Photo-Piezocatalysis	U: 45 kHz L: 300 W (Xe)	0.01492/93.3 (in 180 min)	119
$K_{0.5}Na_{0.5}NbO_3$	RhB	Photo-Piezocatalysis	U: 40 kHz L: 350 W (Xe)	0.0397/92 (in 60 min)	139
$KNbO_3$/ZnO	MO	Photo-Piezocatalysis	U: 120 W, 40 kHz L: 300 W (Xe)	0.06	120
(K, Na)NbO_3	RhB	Piezocatalysis	U: 360 W, 40 kHz	0.091/89 (in 120 min)	93
Ba doped $NaNbO_3$	RhB	Photo-Piezocatalysis	U: 50 W, 40 kHz L: 300 W (Xe)	0.0114/87.5 (in 180 min)	70
Ag dot- $NaNbO_3$	RhB	Photo-Piezocatalysis	U: 200 W, 45 kHz L: 200 W (Xe)	0.16314	133
BiOCl/$NaNbO_3$	RhB	Photo-Piezocatalysis	U: 50 W, 40 kHz L: 300 W (Xe)	0.00192/87.4 (in 100 min)	167
$NaNbO_3$	RhB	Piezocatalysis	U: 150 W, 40 kHz	0.1313	100
CuO/$NaNbO_3$	TC	Photo-Piezocatalysis	U: 200 W, 40 kHz L: 300 W (Xe)	0.012/67 (in 120 min)	168
$MoS_2/NaNbO_3$	MET	Piezocatalysis	U:150 W, 40 kHz	0.012/82.8 (in 160 min)	90
$BiVO_4/NaNbO_3$	TC	Photo-Piezocatalysis	U: 180 W L: 300 W (Xe)	0.028/73.7 (in 60 min)	127
FeCo doped $K_{0.52}Na_{0.48}NbO_3$	RhB	Piezocatalysis	U: 150 W	0.027/95 (in 100 min)	101
$KNbO_3/MoS_2$	RhB Cr(VI) MB	Photo-Piezocatalysis	U:120 W, 40 kHz L: 300 W (Xe)	0.16979/99.99(in 18 min) 0.00877/99.80 (in 12 min) (0.01017)/99.39 (in 16 min)	169
(g-C_3N_4)/$NaNbO_3$	MET	Piezocatalysis	U: 150 W, 40 kHz	0.0138/87.2 (in 160 min)	128
2D/2D $KNbO_3/MoS_2$	TC RhB	Piezocatalysis	U:180 W, 40 kHz	0.085/92.4 (in 30 min) 0.092/94.7 (in 30 min)	169
$KNbO_3/WO_3$	RhB	Photo-Piezocatalysis	U: 120 W, 40 kHz L: 210 W (Xe)	0.0612/99/(in 60 min)	122
$NaNbO_3$/g-C_3N_4	RhB	Photo-Piezocatalysis	U: 180 W, 40 kHz L:300 W (Xe)	0.083/95.9 (in 30 min)	121
$K_{0.48}Na_{0.52}NbO_3$–Fe_2O_3	RhB MO	Piezocatalysis	U: 120, 150, 180 W, 40 kHz	RhB = 0.079/95.1 MO = 0.027/90 (in 40 min)	102
$K_{0.4}Na_{0.6}NbO_3$	MB	Photo-Piezocatalysis	U: 120 W	0.17709/99 (in 40 min)	76
(K, Na)NbO_3	RhB MO	Piezocatalysis	U: 180 W, 40 kHz	RhB = 0.148/99 MO = 0.031/71 (in 40 min)	145
Ag_2O@$KNbO_3$	Orange II	Piezocatalysis	U: 110 W, 40 kHz	0.0349/97.8 (in 120 min)	117
$NaNbO_3$	TC-HCL	Piezocatalysis	U: 120 W, 40 kHz	0.083/99 (in 45 min)	94
$La(Mn_{0.5}Ni_{0.5})O_3$–$NaNbO_3$	RhB	Photo-Piezocatalysis	U: 50 W, 40 kHz L: 300 W (Xe)	0.022/89.7 (in 100 min)	146
$K_{0.5}Na_{0.5}NbO_3$–$Bi_{0.5}Na_{0.5}ZrO_3$	RhB MB Ab10B	Piezocatalysis	U: 300 W, 40 kHz	0.0147/95 (in 180 min) 0.01047/90 (in 180 min) 0.0067/71 (in 180 min)	138
$LiNbO_3$	RhB	Piezocatalysis	U: 180 W, 35 kHz	0.2702/100 (in 20 min)	170
$NaNbO_3/WO_3$	RhB	Photo-Piezocatalysis	U: 180 W, 40 kHz	0.0107/73.7 (in 120 min)	171
(K,Na)NbO_3/CuO	RhB	Photo-Piezocatalysis	U: 300W, 40 kHz L: 100 W (Xe)	0.093/91 (in 25 min)	4

U^*: ultrasonic condition; L^*: light source condition; k^*: reaction rate constant; E^*: efficiency.

clean and sustainable energy source.[147] Piezocatalysts and photo-piezocatalysts have demonstrated the ability to enhance HER by leveraging piezoelectric potential and light energy to facilitate efficient charge separation, driving the reduction of water molecules to produce hydrogen. The conventional HER mechanism involves the following steps:

(i) Charge generation and separation: light irradiation or mechanical stress excites electrons from the valence band (VB) to the conduction band (CB), generating e–h pairs. Simultaneously, mechanical stress induces piezoelectric polarization, creating a built-in electric field that separates these carriers.

(ii) Reduction (hydrogen evolution) and oxidation (oxygen evolution) reactions: electrons migrate to active sites on the catalyst's surface and reduce protons ($2H^+ + 2e \rightarrow H_2$). The conduction band edge must be more negative (higher in energy) than the reduction potential of protons. Holes oxidize water molecules to form oxygen gas and hydroxyl radicals ($H_2O \rightarrow 1/2O_2 + 2H^+ + 2e$). The valence band edge must be more positive (lower in energy) than the oxidation potential of water.

Recently, intermediate water splitting (IWS) has been considered a novel approach for achieving simultaneous hydrogen (H_2) and hydrogen peroxide (H_2O_2) production during piezocatalytic and photo-piezocatalytic processes.[148] Unlike the traditional four-electron overall water splitting ($2H_2O \rightarrow 2H_2 + O_2$), which solely generates H_2 and O_2, IWS is a two-electron process ($2H_2O \rightarrow H_2 + H_2O_2$), which is kinetically favorable. Furthermore, the IWS process can easily separate the products (liquid phase H_2O_2 and gas phase H_2), preventing the reverse reaction.[149]

A study on vanadium-doped $NaNbO_3$ (V-$NaNbO_3$) cubes showed that piezocatalytic hydrogen (H_2) and hydrogen peroxide (H_2O_2) were significantly improved in 10 mol% V-doped $NaNbO_3$ compared to undoped $NaNbO_3$ (Fig. 13(b) and (c)).[150] The piezocatalytic H_2 production rate was increased by 2.2-fold, and the H_2O_2 production rate by 4.6-fold, due to the introduction of vanadium. Vanadium doping caused an increasing the density of active sites and enhanced the piezoelectric response. This resulted in more efficient piezoelectric potential generation under mechanical stress, which improved charge separation and thus boosted hydrogen production. Additionally, the study observed that using 10 mg of the catalyst (as opposed to 50 mg) resulted in a 3.1-fold increase in efficiency, attributed to reduced particle aggregation and a larger effective surface area.

A notable example involves carbon-doped $KNbO_3$ (C-$KNbO_3$) single crystals, which exhibit significantly enhanced piezocatalytic HER performance compared to pristine $KNbO_3$.[151] Carbon doping introduced oxygen vacancies in the crystal lattice and increased polar distortion, as evidenced by density functional theory (DFT) simulations and piezoresponse force microscopy (PFM) measurements. These modifications enhanced the built-in electric field, promoting effective charge separation during piezocatalysis. The optimal composition, 0.5 : 1 C–$KNbO_3$, achieved a hydrogen evolution rate of 524.51 μmol g^{-1} h^{-1} under ultrasonic vibration, nearly doubling the rate of undoped $KNbO_3$. This improved performance was attributed to the reduced reaction barriers for water dissociation and hydrogen generation on the C–$KNbO_3$ surface, as confirmed by DFT calculations.

In another study, a photo-piezocatalytic Au/$AgNbO_3$ system demonstrated a significant improvement in hydrogen production due to the synergy between the LSPR effect of Au and the piezoelectric properties of $AgNbO_3$.[131] The LSPR effect generated hot electrons under light irradiation, which were injected into the CB of $AgNbO_3$. Simultaneously, the piezoelectric potential generated under mechanical stress promoted charge separation, allowing the hot electrons to be efficiently utilized for hydrogen evolution.

These studies highlight the potential of piezocatalysis and photo-piezocatalysis in enhancing HER performance. By improving charge separation and reducing recombination, these systems provide a promising route for scalable hydrogen production in renewable energy applications. Recent studies on piezo- and photo-piezocatalytic HER using KNN-based materials are summarized in Table 2. The CB edges of $KNbO_3$ and $NaNbO_3$ are more negative than the reduction potential of protons (0.0 eV *vs.* NHE), indicating that photogenerated or piezoelectric-induced electrons in the CB have enough energy to reduce H^+ ions into H_2. Despite this favorability for HER, the efficiency of KNN-based materials in HER is often lower than their performance in organic pollutant degradation. This disparity can be attributed to several factors. HER is energy-intensive, requiring multiple electrons and precise reaction kinetics, whereas organic degradation involves simpler oxidative fragmentation. Additionally, HER proceeds through multiple steps, which are slower and require higher activation energy compared to the redox reactions in organic degradation. Furthermore, organic degradation benefits from

Table 2 Summary of hydrogen evolution reactions using KNN-based materials

Materials	Catalysis type	Reaction condition (U^*, L^*)	H_2 production activity (μmol g^{-1} h^{-1})	Ref.
MoS_2 nanosheet-coated $KNbO_3$	Photo-Piezocatalysis	L: 300 W (Xe) U: 110 W, 40 kHz	96.00	27
$KNbO_{3-x}$	Piezocatalysis	Stirring (200 rpm)	3.19 ml g^{-1} h^{-1}	103
C-doped $KNbO_3$	Piezocatalysis	—	524.51	151
V-doped $NaNbO_3$	Piezocatalysis	U: 192 W, 68kHz	346.20	150

U^*: ultrasonic condition; L^*: light source condition.

ROS such as $^{\bullet}OH$ and $^{\bullet}O_2^-$, which rapidly oxidize pollutants, while HER relies solely on charge carriers, lacking direct ROS involvement. To improve HER performance in KNN-based materials, various optimization strategies discussed in this paper could be applied, potentially broadening the applications of KNN-based materials.

5.3. Others

Oxygen evolution reaction. The oxygen evolution reaction (OER) is an essential half-reaction in water splitting, where water molecules are oxidized to produce oxygen gas (O_2).[152] This reaction plays a critical role in applications such as water electrolysis and rechargeable energy storage systems, including metal–air batteries.[153] Both piezocatalysis and photo-piezocatalysis have shown promise in enhancing OER performance by facilitating efficient charge separation and accelerating water oxidation under mechanical or light-induced stimuli. The mechanism of OER involves the following steps:

(i) Charge generation and separation: the light illumination or mechanical stress creates electron–hole pairs. Repeating mechanical vibrations induce piezoelectric potential that drives the separation of electrons and holes.

(ii) Water oxidation reaction: the holes migrate to the catalyst's surface and oxidize water molecules through a series of steps:

$$H_2O + h^+ \rightarrow {}^{\bullet}OH + H^+$$

$$^{\bullet}OH + h^+ \rightarrow O + H^+$$

$$O + O \rightarrow O_2$$

$$\text{Overall reaction}: 2H_2O + 4h^+ \rightarrow O_2 + 4H^+$$

A recent study on $NaNbO_3$/FeOOH composites demonstrated significant improvements in OER performance by combining piezoelectric and photocatalytic mechanisms.[154] The authors used sacrificial agents such as $FeCl_3$ and $AgNO_3$ to address the sluggish four-electron water oxidation process (Fig. 14(a) and (b)). In the presence of $FeCl_3$, the system achieved an oxygen evolution rate of 1155 μmol h^{-1}, primarily due to the reduction of Fe^{3+} to Fe^{2+}, which enhanced hole availability for water oxidation. In contrast, the $AgNO_3$ system showed slightly lower O_2 evolution, attributed to surface deposition of Ag/AgO, which impeded light penetration. The synergy between the piezoelectric potential from $NaNbO_3$ and the optoelectronic properties of FeOOH improved charge sep-

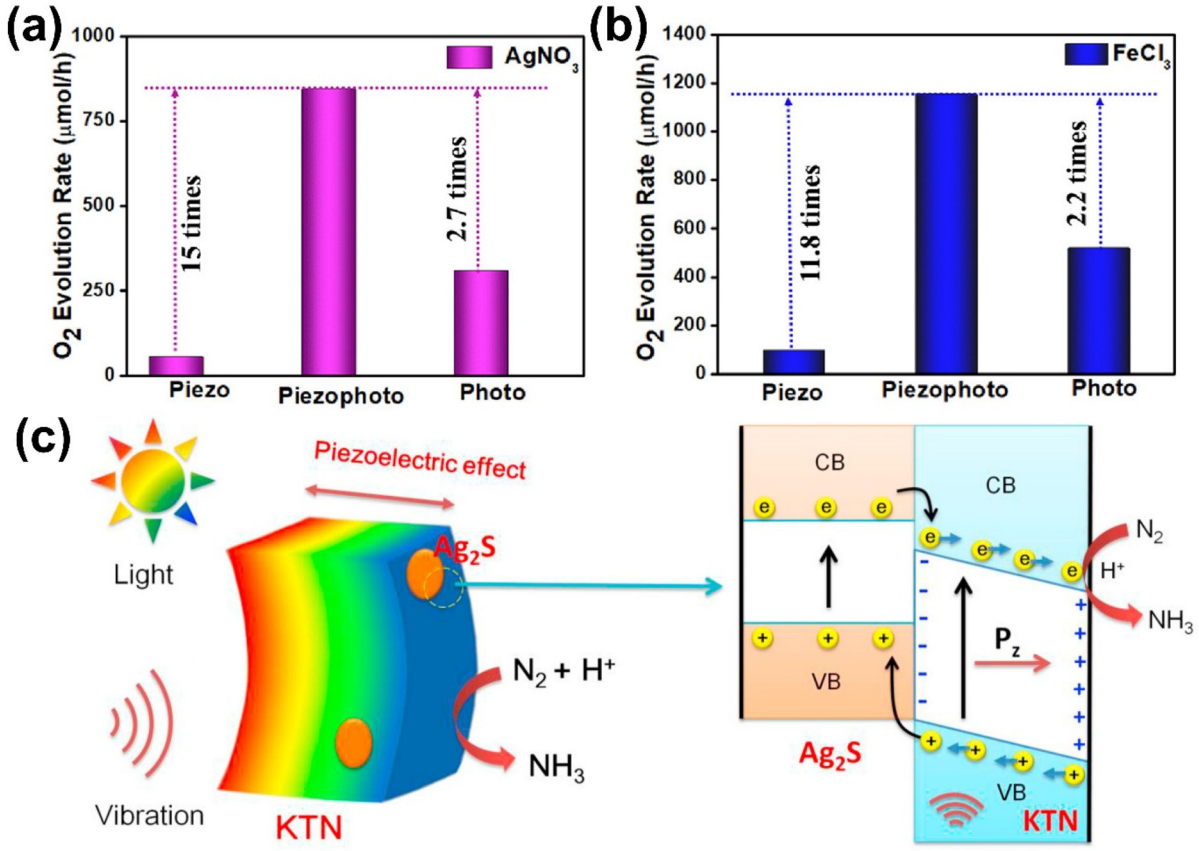

Fig. 14 (a and b) Photo-piezocatalytic oxygen evolution rates over $NaNbO_3$/FeOOH in the presence of (a) $AgNO_3$ and (b) $FeCl_3$ as sacrificial agents. Reprinted with permission from ref. 154. Copyright 2023, American Chemical Society. (c) Schematic illustrations showing the mechanism of photo-piezocatalytic N_2 fixation over Ag_2S/KTN heterojunction. Reprinted with permission from ref. 160. Copyright 2023, Elsevier.

aration and water adsorption. Oxygen vacancies in FeOOH further facilitated the formation of ROS, contributing to efficient water oxidation.

Reduction of carbon dioxide. The reduction of carbon dioxide (CO_2) into valuable chemicals and fuels is another critical application of piezocatalysis and photo-piezocatalysis, addressing both environmental and energy challenges.[155] Piezocatalytic CO_2 reduction converts mechanical energy into surface charges that drive the reduction of CO_2. The mechanism of carbon dioxide reduction reaction (CO_2RR) involves the following steps:

(i) Charge generation and separation: similar to OER, photons and mechanical stimuli excite electrons to the CB, and piezoelectric potential aids in separating these electrons from holes.

(ii) CO_2 adsorption and activation: CO_2 molecules adsorb onto active sites of the catalyst surface, which is activated through bending of the linear molecule, facilitated by electron transfer from the catalyst.

(iii) Stepwise reduction: depending on the catalyst and conditions, the reduction can lead to products like CO, HCOOH, CH_3OH, or CH_4. For example, (iii-a) $CO_2 + 2e^- + 2H^+ \rightarrow CO + H_2O$, (iii-b) $CO + 6e + 6H^+ \rightarrow CH_4 + H_2O$.

A study on KNN-based materials, modified with Li doping to enhance piezoelectric activity, showed promising results in this field.[156] The application of ultrasound generated pressure waves, activating the piezoelectric effect in KNN particles, producing surface charges capable of reducing CO_2 to carbon monoxide (CO). Bicarbonate ions (HCO_3^-) were identified as the active dissolved CO_2 species driving the reduction reaction, with the system showing nearly 100% selectivity for CO production under optimal conditions. The study also examined the impact of CO_2 concentration, catalyst loading, and the use of a hole scavenger to optimize the reduction process.

Nitrogen fixation. Nitrogen fixation, the conversion of nitrogen gas (N_2) into ammonia (NH_3), is essential for fertilizer production and hydrogen storage/transport solutions.[157] Traditional methods like the Haber–Bosch method require high temperatures and pressures, making them energy-intensive and environmentally harmful.[158] Piezocatalysis and photo-piezocatalysis offer greener alternatives by utilizing mechanical energy and light to drive nitrogen fixation under ambient conditions, reducing environmental impact and energy consumption. The mechanism of nitrogen reduction reaction involves the following steps:

(i) Charge generation and separation: photons and mechanical stimuli excite electrons, and piezoelectric potential from mechanical vibrations separates charges effectively.

(ii) N_2 adsorption and activation: N_2 molecules adsorb onto the catalyst surface, in which the strong triple bond in N_2 is weakened through interaction with active sites, facilitated by electron transfer.

(iii) Stepwise protonation and electron transfer: the activated N_2 undergoes stepwise protonation and electron transfer as follows: (iii-a) $N_2 + e + H^+ \rightarrow N_2H_2$, (iii-b) $N_2H_2 + e + H^+ \rightarrow NH_3 + NH_2$, (iii-c) $NH_2 + e + H^+ \rightarrow NH_3$.

Three distinct mechanisms describe the stepwise reduction pathways of N_2. The dissociative pathway involves the dissociation of N_2 molecules into two nitrogen atoms upon adsorption, with each atom undergoing successive hydrogenation to form NH_3. In contrast, the associative distal pathway retains the N_2 molecules intact during adsorption, where protonation and hydrogenation occur sequentially at one nitrogen atom while the other nitrogen atom remains largely unmodified until NH_3 is released. Meanwhile, the associative alternating pathway features alternate protonation and hydrogenation of both nitrogen atoms in the adsorbed N_2 molecule, leading to the stepwise formation of intermediate species.

A study on the piezocatalytic and photopiezocatalytic nitrogen fixation capabilities of CuS/$KTa_{0.75}Nb_{0.25}O_3$ (KTN) nanocomposites demonstrated the effectiveness of combining CuS, an efficient electron acceptor, with the piezoelectric material KTN.[159] Under ultrasonic vibrations, the piezoelectric potential generated in KTN enhanced charge separation and directed electrons toward the CuS active sites, where nitrogen molecules were reduced to ammonia. The system showed a 7.4-fold increase in piezocatalytic NH_3 production compared to KTN alone, highlighting the importance of heterojunction formation. Similarly, a study on Ag_2S/$KTa_{0.5}Nb_{0.5}O_3$ (KTN) heterojunction demonstrated effective nitrogen fixation through a combined photo-piezocatalytic mechanism.[160] The Ag_2S formed a Type-II heterojunction with KTN, facilitating efficient charge separation under both light and mechanical stimulation (Fig. 14(c)). The piezoelectric potential generated in KTN under ultrasonic vibrations worked synergistically with photoexcited electrons from Ag_2S under visible light, significantly increasing NH_3 production.

As another example, the Bi_2S_3/$KTa_{0.75}Nb_{0.25}O_3$ (KTN) nanocomposite demonstrated high efficiency in piezocatalytic nitrogen reduction to ammonia (NH_3).[161] The synergistic interaction between Bi_2S_3 and KTN played a crucial role, with Bi_2S_3 acting as an electron trapper, capturing piezo-induced electrons generated in the KTN phase and effectively preventing electron–hole recombination. This prolonged charge carrier lifetime enhanced catalytic activity. Additionally, Bi_2S_3 significantly improved surface adsorption of N_2, as confirmed by temperature-programmed desorption (TPD) analysis, facilitating N_2 activation and subsequent reduction. Under ultrasonic vibration, the piezoelectric properties of KTN generated an electric field that drove efficient charge separation, with the separated charges participating in the stepwise reduction of N_2 to NH_3. The optimal Bi_2S_3/KTN composite achieved an ammonia production rate of 14.9 μmol g^{-1} h^{-1}, outperforming pure KTN and Bi_2S_3. This study highlights the potential of combining piezoelectric and catalytic synergies for sustainable ammonia synthesis under ambient conditions.

Reduction of heavy metal ions. Heavy metal ion reduction, which converts toxic and soluble metal ions into less toxic or insoluble forms, is crucial for mitigating water contamination and protecting ecosystems. Traditional methods, such as chemical precipitation and adsorption, often suffer from secondary pollution and high energy consumption.[162] In contrast,

advanced techniques like piezocatalysis and photo-piezocatalysis offer eco-friendly and energy-efficient alternatives, utilizing mechanical energy and light under ambient conditions. For instance, $BiFeO_3$@In_2Se_3, $KNbO_3$/MoS_2, and In_2Se_3@SnSe have demonstrated efficient catalytic performance in reducing heavy metal ions such as Cr(VI) and U(VI) into insoluble species in aqueous phases.[163] The reduction mechanism involves photon- and/or mechanical stress-induced electrons, which participate in redox reactions as follows:

$$\text{metal}^{m+} + ne^- \rightarrow \text{metal}^{m-n}$$

In KNN-based systems, $KNbO_3$/MoS_2 (KN–MS) heterojunctions have shown remarkable photo-piezocatalytic performance.[164] These heterojunctions leverage the binary piezoelectric properties of orthorhombic (o-KN) and cubic (c-KN) phases in $KNbO_3$. Among various configurations, the o-KN-MS-3 sample achieved a 99.8% efficiency for Cr(VI) degradation, with a reaction rate constant of 0.00877 min^{-1}, which is 7.9-fold higher than that of c-KN/MS-3 that of KN. In contrast, c-KN/MS-3, which lacks piezoelectric properties, exhibited less than 87% degradation efficiency. This enhanced performance is attributed to the stronger piezoelectric polarization in the binary piezoelectric o-KN/MS heterojunction, which promotes continuous charge carrier separation within o-KN and MoS_2, as well as at their interface. This study highlights the potential of KNN-based piezo- and photo-piezocatalysts in heavy metal remediation, addressing one of the most pressing environmental challenges.

6. Outlook and challenges

In this review, we have highlighted recent advancements in KNN-based piezocatalysis and photo-piezocatalysis, focusing on material design strategies to optimize catalytic performance. We explored the fundamental properties of KNN perovskites, the mechanisms driving piezocatalysis and photo-piezocatalysis, and various optimization strategies such as phase boundary engineering, defect engineering, morphology control, heterojunction formation, and metal deposition/loading. We also discussed key applications, including organic pollutant degradation, hydrogen production, oxygen evolution, CO_2 reduction, and nitrogen fixation. However, as this field progresses, several challenges must be addressed to achieve widespread adoption and scalability of these technologies.

Piezocatalysis and photo-piezocatalysis hold great promise for addressing global challenges in environmental remediation and sustainable energy production. One exciting prospect is using KNN-based piezoelectric materials in self-powered catalytic systems, where mechanical vibrations from natural sources like wind or waves are converted into chemical energy. Such systems could offer environmentally friendly and energy-efficient solutions. The combination of piezoelectric properties with photocatalysis opens avenues for maximizing charge separation and minimizing recombination losses, thus improving catalytic efficiency.

As KNN-based materials evolve, integrating them into renewable energy systems becomes a key research direction. For example, piezoelectric materials could be incorporated into large-scale hydrogen production systems or environmental sensors that harvest mechanical energy from their surroundings. With improved piezoelectric response and light absorption, KNN-based materials have the potential to drive solar-driven processes such as water splitting or CO_2 reduction, making them more practical for renewable energy applications.

Despite the potential, several challenges remain:

6.1 Balancing ferroelectricity and charge carrier concentration

A critical challenge lies in balancing the trade-off between maintaining ferroelectric properties and increasing charge carrier concentrations for efficient catalysis. While KNN materials are insulators, efficient catalysis requires a sufficient number of free-charge carriers. Doping or defect generation can improve catalytic activity, but these often reduce the ferroelectric properties that are essential for generating piezoelectric potential. Future research should focus on developing material designs that maintain a balance between piezoelectricity and charge carrier concentration.

6.2 Understanding fundamental mechanisms

The fundamental mechanisms behind piezocatalysis are still not fully understood. It is particularly important to differentiate piezocatalysis from sonocatalysis, especially in systems that utilize ultrasound. While theories such as energy band theory and screening charge theory explain certain aspects of piezocatalysis, more research is needed to explore the localized surface polarization effects that drive catalytic reactions. Understanding how piezoelectric potential varies at the nanoscale and how it impacts energy band structure and catalytic activity is crucial for future progress.

6.3 Resonance frequency matching

Achieving resonance frequency matching is essential for maximizing the piezoelectric potential generated under mechanical stress. Most current studies use ultrasonic frequencies that do not align with the natural resonance frequencies of the materials, potentially limiting catalytic efficiency. Future research should focus on matching applied frequencies to enhance catalytic activity.

6.4 Material stability and durability

The stability and durability of catalysts under continuous mechanical or light-induced stress present another challenge. Material degradation can reduce the piezoelectric response over time, diminishing catalytic performance. Developing more robust, long-lasting materials through cost-effective production methods will be crucial for large-scale applications. In the case of heterojunction systems, such as S-scheme and metal-decorated configurations, mechanical stress can exacerbate stability issues. Repeated deformation, vibration, or ultra-

sonic stimulation may result in interfacial delamination, phase degradation, or detachment of metal nanoparticles, further impairing performance. Strategies to address these challenges include strengthening mechanical bonds between components and employing robust deposition methods to enhance material durability. Continued advancements in these areas are essential for ensuring the long-term stability of heterojunction-based piezo- and photo-piezocatalytic systems.

6.5 Synergy between piezoelectricity and photocatalysis

The interplay between piezoelectric potential and photocatalytic process is still not fully understood. Future studies should focus on optimizing the synergy to further enhance catalytic performance. This includes investigating how different material designs (*e.g.*, heterojunction formation, defect engineering) can maximize both the piezoelectric effect and light absorption to generate more efficient charge carriers.

To address the challenges, advanced characterization techniques are essential. Real-time, *in situ* measurements of piezoelectric potential, surface polarization, and charge carrier dynamics at the nanoscale will be critical for understanding how these properties evolve during catalytic processes. Additionally, improved methods for distinguishing piezocatalysis from sonocatalysis will help clarify their respective contributions to overall catalytic activity.

There is great potential in designing multifunctional piezo- and photo-piezocatalytic systems that integrate other catalytic mechanisms, such as plasmonic or electrocatalytic processes. For example, combining piezoelectric materials with plasmonic nanoparticles could enhance light absorption and promotes more efficient charge separation. These approaches remain largely unexplored for KNN-based materials.

Finally, further research should explore integrating piezoelectric materials into renewable energy systems. For example, self-powered systems for water splitting or CO_2 reduction that harness mechanical energy from environmental vibrations could provide energy-efficient solutions. Developing scalable and durable KNN-based materials for real-world applications will be essential, including designing materials that maintain their piezoelectric properties under prolonged stress and light exposure, as well as finding cost-effective methods for large-scale production.

Author contributions

Seonhwa Park: conceptualization, investigation, writing – original draft. Hui Yong Jeong: conceptualization, investigation, writing – original draft. Seokhwan Kim: investigation, writing – original draft. Mahesh Peddigari: investigation, writing – original draft. Geon Dae Moon: investigation, writing – original draft, Jong Wook Roh: writing – review & editing, funding acquisition, supervision. Yuho Min: conceptualization, writing – review & editing, project administration, supervision.

Data availability

No primary research results, software, or code have been included and no new data were generated or analyzed as part of this review.

Conflicts of interest

There are no conflicts to declare.

Acknowledgements

This work was supported by the National Research Foundation of Korea (NRF) grant funded by the Ministry of Science and ICT (2021R1A5A8033165 and RS-2023-00241159).

References

1 D.-S. Park, M. Hadad, L. M. Riemer, R. Ignatans, D. Spirito, V. Esposito, V. Tileli, N. Gauquelin, D. Chezganov, D. Jannis, J. Verbeeck, S. Gorfman, N. Pryds, P. Muralt and D. Damjanovic, *Science*, 2022, **375**, 653–657.
2 G. Huangfu, K. Zeng, B. Wang, J. Wang, Z. Fu, F. Xu, S. Zhang, H. Luo, D. Viehland and Y. Guo, *Science*, 2022, **378**, 1125–1130.
3 Y. Liu, J. Fan, X. Qi, B. Shen, R. Zhang and K. Yao, *Nano Energy*, 2024, **128**, 109972.
4 E. Im, S. Park, G.-T. Hwang, D. C. Hyun, Y. Min and G. D. Moon, *Small*, 2024, **20**, 2304360.
5 H. Xiao, W. Dong, Q. Zhao, F. Wang and Y. Guo, *J. Hazard. Mater.*, 2021, **416**, 125808.
6 J. Wang, C. Hu, L. Shi, N. Tian, H. Huang, H. Ou and Y. Zhang, *J. Mater. Chem. A*, 2021, **9**, 12400–12432.
7 L. Chen, J.-T. Ren and Z.-Y. Yuan, *Adv. Energy Mater.*, 2023, **13**, 2203720.
8 A. Zhang, Z. Liu, B. Xie, J. Lu, K. Guo, S. Ke, L. Shu and H. Fan, *Appl. Catal., B*, 2020, **279**, 119353.
9 X. Zhou, B. Shen, A. Lyubartsev, J. Zhai and N. Hedin, *Nano Energy*, 2022, **96**, 107141.
10 S. Xu, W. Qian, D. Zhang, X. Zhao, X. Zhang, C. Li, C. R. Bowen and Y. Yang, *Nano Energy*, 2020, **77**, 105305.
11 H. Zhai, H. Liu, Y. Zhang, J. Tong, X. Liu, W. Du, H. Liao, P. Tan and J. Pan, *Appl. Catal., B*, 2024, **349**, 123909.
12 J. Koruza, H. Liu, M. Höfling, M.-H. Zhang and P. Veber, *J. Mater. Res.*, 2020, **35**, 990–1016.
13 X. Lv, J. Zhu, D. Xiao, X.-x. Zhang and J. Wu, *Chem. Soc. Rev.*, 2020, **49**, 671–707.
14 Z. Zhang, W. Wang, L. Wang and S. Sun, *ACS Appl. Mater. Interfaces*, 2012, **4**, 593–597.
15 Y. Wen, J. Chen, X. Gao, H. Che, P. Wang, B. Liu and Y. Ao, *Nano Energy*, 2022, **101**, 107614.
16 C. Zhao, C. Wang, X. Ren, S. Yuan, L. Zhao, L. Zhuang, B. Teng, Y. Wu and Y. He, *Chem. Eng. J.*, 2024, **498**, 155202.

17 S. Li, Z. Zhao, D. Yu, J.-Z. Zhao, Y. Su, Y. Liu, Y. Lin, W. Liu, H. Xu and Z. Zhang, *Nano Energy*, 2019, **66**, 104083.
18 P. Zhu, Y. Chen and J. Shi, *Adv. Mater.*, 2020, **32**, 2001976.
19 O. Amiri, K. Salar, P. Othman, T. Rasul, D. Faiq and M. Saadat, *J. Hazard. Mater.*, 2020, **394**, 122514.
20 S. Verma, M. Sharma, A. Halder and R. Vaish, *Surf. Interfaces*, 2022, **30**, 101827.
21 X. Liu, M. Wang, Y. Zhou, T. Li, H. Duan, J. Li, L. Wang, Y. Li, S. Yang, J. Wu, C. Wang, X. Feng and F. Li, *Small*, 2023, **19**, 2303129.
22 K. T. Wong, C. E. Choong, I. W. Nah, S.-H. Kim, B.-H. Jeon, Y. Yoon, E. H. Choi and M. Jang, *Appl. Catal., B*, 2022, **315**, 121581.
23 M.-L. Xu, M. Lu, G.-Y. Qin, X.-M. Wu, T. Yu, L.-N. Zhang, K. Li, X. Cheng and Y.-Q. Lan, *Angew. Chem., Int. Ed.*, 2022, **61**, e202210700.
24 Y. Wang, H. Ma, J. Liu, Z. Zhang, Y. Yu and S. Zuo, *J. Colloid Interface Sci.*, 2024, **665**, 655–680.
25 Y. Fu, Z. Ren, J. Wu, Y. Li, W. Liu, P. Li, L. Xing, J. Ma, H. Wang and X. Xue, *Appl. Catal., B*, 2021, **285**, 119785.
26 S. Lu, S. Zhang, L. Li, C. Liu, Z. Li and D. Luo, *Chem. Eng. J.*, 2024, **483**, 149058.
27 S. Jia, Y. Su, B. Zhang, Z. Zhao, S. Li, Y. Zhang, P. Li, M. Xu and R. Ren, *Nanoscale*, 2019, **11**, 7690–7700.
28 S. Zhong, Y. Wang, Y. Chen, X. Jiang, M. Lin, C. Lin, T. Lin, M. Gao, C. Zhao and X. Wu, *Chem. Eng. J.*, 2024, **488**, 151002.
29 D. Liu, C. Jin, F. Shan, J. He and F. Wang, *ACS Appl. Mater. Interfaces*, 2020, **12**, 17443–17451.
30 C. Yu, M. Tan, Y. Li, C. Liu, R. Yin, H. Meng, Y. Su, L. Qiao and Y. Bai, *J. Colloid Interface Sci.*, 2021, **596**, 288–296.
31 P. Wang, W. Cai, F. Yu, P. Zhou, M. Lin, C. Lin, T. Lin, M. Gao, C. Zhao, X. Li and X. Wu, *Chemosphere*, 2023, **338**, 139548.
32 K. Zhou, W. Liu, P. Wang, J. Chen, H. Che, B. Liu and Y. Ao, *Chem. Eng. J.*, 2024, **480**, 148012.
33 E. Lin, Z. Kang, J. Wu, R. Huang, N. Qin and D. Bao, *Appl. Catal., B*, 2021, **285**, 119823.
34 G. Yang, Q. Chen, W. Wang, S. Wu, B. Gao, Y. Xu, Z. Chen, S. Zhong, J. Chen and S. Bai, *ACS Appl. Mater. Interfaces*, 2021, **13**, 15305–15314.
35 P. Wang, X. Li, S. Fan, X. Chen, M. Qin, D. Long, M. O. Tadė and S. Liu, *Appl. Catal., B*, 2020, **279**, 119340.
36 Y. Jiang, C. Y. Toe, S. S. Mofarah, C. Cazorla, S. L. Y. Chang, Y. Yin, Q. Zhang, S. Lim, Y. Yao, R. Tian, Y. Wang, T. Zaman, H. Arandiyan, G. G. Andersson, J. Scott, P. Koshy, D. Wang and C. C. Sorrell, *ACS Sustainable Chem. Eng.*, 2023, **11**, 3370–3389.
37 R. Su, H. A. Hsain, M. Wu, D. Zhang, X. Hu, Z. Wang, X. Wang, F.-t. Li, X. Chen, L. Zhu, Y. Yang, Y. Yang, X. Lou and S. J. Pennycook, *Angew. Chem., Int. Ed.*, 2019, **58**, 15076–15081.
38 T. He, Z. Cao, G. Li, Y. Jia and B. Peng, *J. Adv. Ceram.*, 2022, **11**, 1641–1653.
39 R. Su, Z. Wang, L. Zhu, Y. Pan, D. Zhang, H. Wen, Z.-D. Luo, L. Li, F.-t. Li, M. Wu, L. He, P. Sharma and J. Seidel, *Angew. Chem., Int. Ed.*, 2021, **60**, 16019–16026.
40 H. Yu, X. Wei, M. Wang, Y. Zhang, Z. Wu, F. Guo and J. Han, *J. Adv. Ceram.*, 2024, **13**, 437–446.
41 C. Yu, J. He, M. Tan, Y. Hou, H. Zeng, C. Liu, H. Meng, Y. Su, L. Qiao, T. Lookman and Y. Bai, *Adv. Funct. Mater.*, 2022, **32**, 2209365.
42 A. D. Mani, J. Li, Z. Wang, J. Zhou, H. Xiang, J. Zhao, L. Deng, H. Yang and L. Yao, *J. Adv. Ceram.*, 2022, **11**, 1069–1081.
43 C. Meng, Z. Wang, L. Zhang, X. Ji, X. Chen and R. Yu, *Inorg. Chem.*, 2022, **61**, 9832–9839.
44 Q. Zhao, Y. Yang, G. Xiong, J. Chen, T. Xu, Q. Xu, R. Zhang, W. Yao, H. Li and C.-S. Lee, *J. Am. Chem. Soc.*, 2024, **146**, 16648.
45 R. Guo, X. Zhang, Y. Chen and Y. Zhang, *Adv. Funct. Mater.*, 2024, **34**, 2408838.
46 K. Wang, C. Han, J. Li, J. Qiu, J. Sunarso and S. Liu, *Angew. Chem.*, 2022, **134**, e202110429.
47 N. Meng, W. Liu, R. Jiang, Y. Zhang, S. Dunn, J. Wu and H. Yan, *Prog. Mater. Sci.*, 2023, **138**, 101161.
48 F. Bößl and I. Tudela, *Curr. Opin. Green Sustainable Chem.*, 2021, **32**, 100537.
49 P. Jia, J. Li and H. Huang, *Adv. Funct. Mater.*, 2024, **34**, 2407309.
50 H. Zheng, Y. Wang, J. Liu, J. Wang, K. Yan and K. Zhu, *Appl. Catal., B*, 2024, **341**, 123335.
51 C. Wang, C. Hu, F. Chen, T. Ma, Y. Zhang and H. Huang, *Nano Energy*, 2023, **107**, 108093.
52 S. Tu, Y. Guo, Y. Zhang, C. Hu, T. Zhang, T. Ma and H. Huang, *Adv. Funct. Mater.*, 2020, **30**, 2005158.
53 H. Dong, Y. Zhou, L. Wang, L. Chen and M. Zhu, *Chem. Eng. J.*, 2024, **487**, 150480.
54 W. Dong, H. Xiao, Y. Jia, L. Chen, H. Geng, S. U. H. Bakhtiar, Q. Fu and Y. Guo, *Adv. Sci.*, 2022, **9**, 2105368.
55 S. S. Jeyabalan, O. S. Ekande, B. Mainali and M. Kumar, *Chem. Eng. J.*, 2024, **498**, 155086.
56 P. Dhiman, J. Sharma, A. Kumar, G. Sharma, G. Rana and G. T. Mola, *Mater. Today Sustain.*, 2024, **28**, 100973.
57 M. Du, W. Liu, N. Liu, Y. Ling and S. Kang, *Nano Energy*, 2024, **124**, 109495.
58 S. Chen, P. Zhu, L. Mao, W. Wu, H. Lin, D. Xu, X. Lu and J. Shi, *Adv. Mater.*, 2023, **35**, 2208256.
59 X. Yuan, J. Shi, Y. Kang, J. Dong, Z. Pei and X. Ji, *Adv. Mater.*, 2024, **36**, 2308726.
60 L. Wang, S. Zhang, Y. Zhang and Q. An, *Nano Energy*, 2023, **110**, 108342.
61 Z. Liang, C.-F. Yan, S. Rtimi and J. Bandara, *Appl. Catal., B*, 2019, **241**, 256–269.
62 J. Liu, W. Qi, M. Xu, T. Thomas, S. Liu and M. Yang, *Angew. Chem.*, 2023, **135**, e202213927.
63 Y. Bao, K. Xiao, S. Yue, M. Zhang, X. Du, J. Wang, W.-D. Oh, Y. Zhou and S. Zhan, *Surf. Interfaces*, 2023, **40**, 103107.

64 F. Yang, P. Wang, J. Hao, J. Qu, Y. Cai, X. Yang, C. M. Li and J. Hu, *Nano Energy*, 2023, **118**, 108993.
65 L. Chen, Y. Yang, S. Jiang, B. Yang and W. Rao, *Mater. Today Chem.*, 2023, **30**, 101486.
66 S. Mansingh, N. Priyadarshini, J. Panda, K. K. Das, D. P. Sahoo, J. Sahu, D. Prusty, R. K. Giri, A. Mishra and K. Parida, *Energy Fuels*, 2024, **38**, 5632–5658.
67 H. Sudrajat, I. Rossetti and J. C. Colmenares, *J. Mater. Chem. A*, 2023, **11**, 24566–24590.
68 S. Park, C. W. Lee, M.-G. Kang, S. Kim, H. J. Kim, J. E. Kwon, S. Y. Park, C.-Y. Kang, K. S. Hong and K. T. Nam, *Phys. Chem. Chem. Phys.*, 2014, **16**, 10408–10413.
69 G. Mamba, P. J. Mafa, V. Muthuraj, A. Mashayekh-Salehi, S. Royer, T. I. T. Nkambule and S. Rtimi, *Mater. Today Nano*, 2022, **18**, 100184.
70 L. Li, W. Cao, W. Liu, C. Liang, X. Shi, F. Li and C. Wang, *Ceram. Int.*, 2022, **48**, 36908–36916.
71 S.-H. V. Oh, W. Hwang, K. Kim, J.-H. Lee and A. Soon, *Adv. Sci.*, 2022, **9**, 2104569.
72 V. M. Goldschmidt, *Naturwissenschaften*, 1926, **14**, 477–485.
73 H. Du, W. Zhou, F. Luo, D. Zhu, S. Qu and Z. Pei, *J. Appl. Phys.*, 2008, **104**, 044104.
74 J.-F. Li, K. Wang, F.-Y. Zhu, L.-Q. Cheng and F.-Z. Yao, *J. Am. Ceram. Soc.*, 2013, **96**, 3677–3696.
75 S. Park, M. Peddigari, J. H. Kim, E. Kim, G.-T. Hwang, J.-W. Kim, C.-W. Ahn, J.-J. Choi, B.-D. Hahn, J.-H. Choi, W.-H. Yoon, D.-S. Park, K.-I. Park, C. K. Jeong, J. W. Lee and Y. Min, *Inorg. Chem.*, 2020, **59**, 3042–3052.
76 R. Guo, M. Liu, Y. Xing, T. Bai, C. Zhao, H. Huang and H. Zhang, *Nanoscale*, 2023, **15**, 6920–6933.
77 T. Zheng, J. Wu, D. Xiao and J. Zhu, *Prog. Mater. Sci.*, 2018, **98**, 552–624.
78 O. Tokay and M. Yazıcı, *Mater. Today Commun.*, 2022, **31**, 103358.
79 P. Li, J. Zhai, B. Shen, S. Zhang, X. Li, F. Zhu and X. Zhang, *Adv. Mater.*, 2018, **30**, 1705171.
80 S. Park, J. Jang, C.-W. Ahn, B.-D. Hahn, W.-H. Yoon, J. W. Lee, J.-J. Choi and Y. Min, *J. Eur. Ceram. Soc.*, 2023, **43**, 1932–1940.
81 F. Li, M. J. Cabral, B. Xu, Z. Cheng, E. C. Dickey, J. M. LeBeau, J. Wang, J. Luo, S. Taylor, W. Hackenberger, L. Bellaiche, Z. Xu, L.-Q. Chen, T. R. Shrout and S. Zhang, *Science*, 2019, **364**, 264–268.
82 S. Park, H. Choi, G.-T. Hwang, M. Peddigari, C.-W. Ahn, B.-D. Hahn, W.-H. Yoon, J. W. Lee, K.-I. Park, J. Jang, J.-J. Choi and Y. Min, *ACS Nano*, 2022, **16**, 15328–15338.
83 M. B. Starr and X. Wang, *Sci. Rep.*, 2013, **3**, 2160.
84 F. Bößl, V. C. Menzel, K. Jeronimo, A. Arora, Y. Zhang, T. P. Comyn, P. Cowin, C. Kirk, N. Robertson and I. Tudela, *Electrochim. Acta*, 2023, **462**, 142730.
85 J. E. Garcia and F. Rubio-Marcos, *J. Appl. Phys.*, 2020, **127**, 131102.
86 Z. Dai, D. Li, Z. Zhou, S. Zhou, W. Liu, J. Liu, X. Wang and X. Ren, *Chem. Eng. J.*, 2022, **427**, 131959.
87 Y. Liu, H.-Y. Xu and S. Komarneni, *Appl. Catal., A*, 2024, **670**, 119550.
88 S. Merouani, O. Hamdaoui, Y. Rezgui and M. Guemini, *Ultrason. Sonochem.*, 2014, **21**, 53–59.
89 M. B. Starr and X. Wang, *Nano Energy*, 2015, **14**, 296–311.
90 O. S. Ekande and M. Kumar, *Chem. Eng. J.*, 2023, **458**, 141454.
91 Z. Cen, Y. Zhen, W. Feng, P. Zhao, L. Chen, C. Zhu, X. Wang and L. Li, *J. Am. Ceram. Soc.*, 2018, **101**, 4108–4117.
92 R. Li, X.-X. Sun, X. Lv, T. Zheng and J. Wu, *Acta Mater.*, 2021, **218**, 117229.
93 X.-x. Sun, R. Li, Z. Yang, N. Zhang, C. Wu, J. Li, Y. Chen, Q. Chen, J. Zhang, H. Yan, X. Lv and J. Wu, *Appl. Catal., B*, 2022, **313**, 121471.
94 Y. Yi, M. Wu, R. Wang, Q. He, P. Sun, B. Zhou and X. Dong, *Chem. Eng. J.*, 2024, **485**, 149885.
95 Y. Min, M. Kim, G.-T. Hwang, C.-W. Ahn, J.-J. Choi, B.-D. Hahn, W.-H. Yoon, G. D. Moon, C.-S. Park and C.-H. Park, *Nano Energy*, 2020, **78**, 105198.
96 Y. Long, H. Xu, J. He, C. Li and M. Zhu, *Surf. Interfaces*, 2022, **31**, 102056.
97 Y. Li, M. Borbely and A. Bell, *J. Am. Ceram. Soc.*, 2021, **104**, 2678–2688.
98 Y. Sheng, Y. Huang, C. Chen, M. Zhang, N. Deng and L. Ma, *Ceram. Int.*, 2018, **44**, 10141–10146.
99 L. Sun, J. Hu, H. Qin, M. Zhao and K. Fan, *J. Phys. Chem. C*, 2011, **115**, 5593–5598.
100 T. Yang, P. Ren, X. Qi, X. Wang, Q. Meng, Z. Liu and S. Yang, *Appl. Surf. Sci.*, 2023, **628**, 157363.
101 M. Zhou, L. Liang, D. Lu, X. Lu, Z. Wang, F. Huang, P. Cheng, D. Liu, M. Tian, Q. Wang and Y. Zhang, *Int. J. Miner., Metall. Mater.*, 2023, **30**, 2044–2054.
102 J. Liao, X. Lv, J. Zheng, H. Wang, Q. Chen, D. Gao, J. Bi and J. Wu, *Mater. Today Commun.*, 2023, **37**, 107564.
103 H.-Y. Tan, L. Zhan, C.-F. Yan, L. K. Abeykoon, N. L. D. Silva and J. Bandara, *Nano Express*, 2020, **1**, 030036.
104 A. Rovisco, R. Branquinho, J. Deuermeier, T. Freire, E. Fortunato, R. Martins and P. Barquinha, *ACS Appl. Nano Mater.*, 2021, **4**, 1149–1161.
105 Q. Tang, J. Wu, D. Kim, C. Franco, A. Terzopoulou, A. Veciana, J. Puigmartí-Luis, X.-Z. Chen, B. J. Nelson and S. Pané, *Adv. Funct. Mater.*, 2022, **32**, 2202180.
106 M. Dai, W. Zheng, X. Zhang, S. Wang, J. Lin, K. Li, Y. Hu, E. Sun, J. Zhang, Y. Qiu, Y. Fu, W. Cao and P. Hu, *Nano Lett.*, 2020, **20**, 201–207.
107 D. Yu, Z. Liu, J. Zhang, S. Li, Z. Zhao, L. Zhu, W. Liu, Y. Lin, H. Liu and Z. Zhang, *Nano Energy*, 2019, **58**, 695–705.
108 Z. L. Wang, *Nano Today*, 2010, **5**, 540–552.
109 M. Wang, B. Wang, F. Huang and Z. Lin, *Angew. Chem., Int. Ed.*, 2019, **58**, 7526–7536.
110 X. Xu, Y. Wang, W. Cheng, H. Zhai, L. Xiao, L. Qin and D. Chen, *Surf. Interfaces*, 2024, **54**, 105245.
111 P. Hao, Y. Cao, X. Ning, R. Chen, J. Xie, J. Hu, Z. Lu and A. Hao, *J. Colloid Interface Sci.*, 2023, **639**, 343–354.

112 K. Wang, B. Li, C. Zhao, S. Yuan, C. Zhang, X. Liang, J. Wang, Y. Wu and Y. He, *Ultrason. Sonochem.*, 2023, **92**, 106285.
113 Z. Kang, K. Ke, E. Lin, N. Qin, J. Wu, R. Huang and D. Bao, *J. Colloid Interface Sci.*, 2022, **607**, 1589–1602.
114 S. Atif, D. A. Afzal, L. Abdelkader, X. Li, Q. Dong and C. Wang, *J. Catal.*, 2023, **428**, 115179.
115 D. Salazar-Marín, G. Oza, J. A. D. Real, A. Cervantes-Uribe, H. Pérez-Vidal, M. K. Kesarla, J. G. T. Torres and S. Godavarthi, *Appl. Surf. Sci. Adv.*, 2024, **19**, 100536.
116 T. Yin, L. Long, X. Tang, M. Qiu, W. Liang, R. Cao, Q. Zhang, D. Wang and H. Zhang, *Adv. Sci.*, 2020, **7**, 2001431.
117 R. Li, Y. Cai, S. Liang, A. Aihemaiti and Z. Zhang, *Appl. Surf. Sci.*, 2024, **644**, 158811.
118 T. Teranishi and M. Sakamoto, *J. Phys. Chem. Lett.*, 2013, **4**, 2867–2873.
119 Y. Zhang, G. Shen, C. Sheng, F. Zhang and W. Fan, *Appl. Surf. Sci.*, 2021, **562**, 150164.
120 Y. Li, H. Chen, L. Wang, T. Wu, Y. Wu and Y. He, *Ultrason. Sonochem.*, 2021, **78**, 105754.
121 X. Yan, M. Xie, L. Pan, T. Ai, Z. Li and Y. Niu, *J. Mater. Sci.: Mater. Electron.*, 2023, **34**, 695.
122 R. Huang, W. Cai, H. Zhang, Z. Wang, Q. Zhang, R. Gao, G. Chen, X. Deng, X. Lei, J. Dong, X. Liu and C. Fu, *J. Environ. Chem. Eng.*, 2023, **11**, 110177.
123 S. Dharani, S. Vadivel, L. Gnanasekaran and S. Rajendran, *Fuel*, 2023, **349**, 128688.
124 A. Shabbir, S. Sardar and S. Mumtaz, *J. Alloys Compd.*, 2024, **1003**, 175683.
125 Q. Xu, L. Zhang, B. Cheng, J. Fan and J. Yu, *Chem*, 2020, **6**, 1543–1559.
126 M. E. Malefane, J. T. Khutlane, M. Managa, C. G. C. E. van Sittert, T. T. I. Nkambule and A. T. Kuvarega, *Adv. Compos. Hybrid Mater.*, 2024, **7**, 181.
127 M. Lv, H. Wang and H. Shi, *Colloids Surf., A*, 2023, **679**, 132579.
128 O. S. Ekande and M. Kumar, *J. Colloid Interface Sci.*, 2023, **651**, 477–493.
129 Y. Zhu, H. Chen, L. Wang, L. Ye, H. Zhou, Q. Peng, H. Zhu and Y. Huang, *Chin. Chem. Lett.*, 2024, **35**, 108884.
130 S. Kim, J. W. Roh, D. C. Hyun, S. Park and Y. Min, *J. Korean Inst. Electr. Electron. Mater. Eng.*, 2024, **37**, 547–553.
131 S. Li, Z. Zhao, M. Liu, X. Liu, W. Huang, S. Sun, Y. Jiang, Y. Liu, J. Zhang and Z. Zhang, *Nano Energy*, 2022, **95**, 107031.
132 H. Meng, Z. Chen, Z. Lu and X. Wang, *J. Mol. Liq.*, 2023, **369**, 120846.
133 Q. Sun, D. Zhang, G. Xue, Q. Liu, X. Zhou, Z. Pei, H. Luo and L. Zhu, *Ceram. Int.*, 2022, **48**, 23182–23194.
134 L. Yan, T. Zhang, W. Lei, Q. Xu, X. Zhou, P. Xu, Y. Wang and G. Liu, *Catal. Today*, 2014, **224**, 140–146.
135 Q. Liu, Y. Chai, L. Zhang, J. Ren and W.-L. Dai, *Appl. Catal., B*, 2017, **205**, 505–513.
136 P. Kumar, R. Vaish, T. H. Sung, W. Hwang, H. K. B. Park, A. Kumar, I. Kebaili and I. Boukhris, *Glob. Chall.*, 2023, **7**, 2200142.
137 G.-T. Hwang, V. Annapureddy, J. H. Han, D. J. Joe, C. Baek, D. Y. Park, D. H. Kim, J. H. Park, C. K. Jeong, K.-I. Park, J.-J. Choi, D. K. Kim, J. Ryu and K. J. Lee, *Adv. Energy Mater.*, 2016, **6**, 1600237.
138 Z. Xie, J. Jiao, M. Hu, C. Zhao, X. Wu, T. Lin, M. Gao and C. Lin, *J. Am. Ceram. Soc.*, 2024, **107**, 5512–5523.
139 M. Lun, X. Zhou, S. Hu, Y. Hong, B. Wang, A. Yao, W. Li, B. Chu, Q. He, J. Cheng and Y. Wang, *Ceram. Int.*, 2021, **47**, 28797–28805.
140 W. Zheng, Y. Tang, C. Jia, Z. Liu, Z. Zhang and K. Zhao, *J. Mater. Chem. A*, 2024, **12**, 11378–11389.
141 J. Li, X. Liu, G. Zhao, Z. Liu, Y. Cai, S. Wang, C. Shen, B. Hu and X. Wang, *Sci. Total Environ.*, 2023, **869**, 161767.
142 A. Mishra, M. Kumari, Swati, R. Kumar, K. Iqbal and I. S. Thakur, *Bioresour. Technol. Rep.*, 2022, **19**, 101143.
143 L. Xu and L. Liu, *Appl. Catal., B*, 2021, **304**, 120953.
144 S. Wacławek, H. V. Lutze, K. Grübel, V. V. T. Padil, M. Černík and D. D. Dionysiou, *Chem. Eng. J.*, 2017, **330**, 44–62.
145 X. Wang, N. Wang, J. Liao, X. Wang, A. Zou, Q. Chen, C.-B.-W. Li, J. Zhang, D. Wang, Y. Peng, X. Lv and J. Wu, *Adv. Funct. Mater.*, 2024, **34**, 2313662.
146 L. Li, S. Lu, W. Cao, Q. Zhu, R. Li, Y. Wei, S. Yang and C. Wang, *Inorg. Chem.*, 2024, **63**, 11745–11756.
147 A. Kazemi, F. Manteghi and Z. Tehrani, *ACS Omega*, 2024, **9**, 7310–7335.
148 S. Cao, T.-S. Chan, Y.-R. Lu, X. Shi, B. Fu, Z. Wu, H. Li, K. Liu, S. Alzuabi, P. Cheng, M. Liu, T. Li, X. Chen and L. Piao, *Nano Energy*, 2020, **67**, 104287.
149 S. Cao, T. Sun, Y. Peng, X. Yu, Q. Li, F. L. Meng, F. Yang, H. Wang, Y. Xie, C.-C. Hou and Q. Xu, *Small*, 2024, **20**, 2404285.
150 Y. Li, L. Li, F. Liu, B. Wang, F. Gao, C. Liu, J. Fang, F. Huang, Z. Lin and M. Wang, *Nano Res.*, 2022, **15**, 7986–7993.
151 J. He, F. Gao, H. Wang, F. Liu, J. Lin, B. Wang, C. Liu, F. Huang, Z. Lin and M. Wang, *Environ. Sci.: Nano*, 2022, **9**, 1952–1960.
152 L. Chen, Y. Wang, X. Zhao, Y. Wang, Q. Li, Q. Wang, Y. Tang and Y. Lei, *J. Mater. Sci. Technol.*, 2022, **110**, 128–135.
153 M. A. Alemu, A. K. Worku and M. Z. Getie, *Inorg. Chem. Commun.*, 2024, **159**, 111742.
154 N. Priyadarshini, S. Mansingh, K. K. Das, R. Garg, Sumit, K. Parida and K. Parida, *Inorg. Chem.*, 2024, **63**, 256–271.
155 Q. Xu, J. Jiang, X. Sheng, Q. Jing, X. Wang, L. Duan and H. Guo, *Inorg. Chem. Front.*, 2023, **10**, 2939–2950.
156 P. T. T. Phuong, D.-V. N. Vo, N. P. H. Duy, H. Pearce, Z. M. Tsikriteas, E. Roake, C. Bowen and H. Khanbareh, *Nano Energy*, 2022, **95**, 107032.
157 J. Islam, M. Shareef, H. M. Zabed, X. Qi, F. I. Chowdhury, J. Das, J. Uddin, Y. V. Kaneti, M. U. Khandaker, M. H. Ullah and M. K. Masud, *Energy Storage Mater.*, 2023, **54**, 98–119.

158 A. Vojvodic, A. J. Medford, F. Studt, F. Abild-Pedersen, T. S. Khan, T. Bligaard and J. K. Nørskov, *Chem. Phys. Lett.*, 2014, **598**, 108–112.
159 X. Dai, L. Chen, Z. Li, X. Li, J. Wang, X. Hu, L. Zhao, Y. Jia, S.-X. Sun, Y. Wu and Y. He, *J. Colloid Interface Sci.*, 2021, **603**, 220–232.
160 L. Chen, J. Wang, X. Li, J. Zhang, C. Zhao, X. Hu, H. Lin, L. Zhao, Y. Wu and Y. He, *Green. Energy Environ.*, 2023, **8**, 1630–1643.
161 L. Chen, X. Dai, X. Li, J. Wang, H. Chen, X. Hu, H. Lim, Y. He, Y. Wu and M. Fan, *J. Mater. Chem. A*, 2021, **9**, 13344.
162 Y. Fei and Y. H. Hu, *Chemosphere*, 2023, **335**, 139077.
163 R. Guo, L. Jin and Y. Zhang, *Small*, 2024, **20**, 2307946.
164 W. Ma, M. Du, H. Li, Y. Wang, Z. Han, C. Chen, S. Zhang, Q. Han, Y. Li, J. Fang and P. Fang, *J. Alloys Compd.*, 2023, **960**, 170669.
165 A. Zhang, Z. Liu, X. Geng, W. Song, J. Lu, B. Xie, S. Ke and L. Shu, *Ceram. Int.*, 2019, **45**, 22486–22492.
166 H. You, X. Ma, Z. Wu, L. Fei, X. Chen, J. Yang, Y. Liu, Y. Jia, H. Li, F. Wang and H. Huang, *Nano Energy*, 2018, **52**, 351–359.
167 L. Li, W. Cao, J. Yao, W. Liu, F. Li and C. Wang, *Nanomaterials*, 2022, **12**, 353.
168 H. Wang, H. Zhang, Z. Long and H. Shi, *Catal. Sci. Technol.*, 2023, **13**, 2239–2246.
169 H. Luo, Z. Liu, C. Ma, A. Zhang, Q. Zhang and F. Wang, *J. Environ.*, 2023, **11**, 111521.
170 D. Jiang, W. Chen, Y. Duan, Z. Li, Z. Xiao, Y. Jing, Q. Ye, L. Zhou, M. Wang and J. Cai, *J. Phys. Chem. Solids*, 2024, **184**, 111692.
171 X. Yan, S. Zhang, L. Pan, T. Ai, Z. Li and Y. Niu, *Inorg. Chem. Commun.*, 2023, **158**, 111510.